Lawrence Berkeley National Laboratory
LBL Publications

Title
Thickness Dependence of Proton-Exchange-Membrane Properties

Permalink
https://escholarship.org/uc/item/5jf4z61g

Journal
Journal of The Electrochemical Society, 168(10)

ISSN
0013-4651

Authors
Luo, Xiaoyan
Lau, Grace
Tesfaye, Meron
et al.

Publication Date
2021-10-01

DOI
10.1149/1945-7111/ac2973

Peer reviewed

eScholarship.org Powered by the California Digital Library
University of California

Journal of The Electrochemical Society

The Electrochemical Society
Advancing solid state & electrochemical science & technology

OPEN ACCESS

Thickness Dependence of Proton-Exchange-Membrane Properties

To cite this article: Xiaoyan Luo *et al* 2021 *J. Electrochem. Soc.* **168** 104517

View the article online for updates and enhancements.

This content was downloaded from IP address 104.186.254.98 on 01/12/2022 at 22:29

Journal of The Electrochemical Society, 2021 **168** 104517

Thickness Dependence of Proton-Exchange-Membrane Properties

Xiaoyan Luo,[1,a] Grace Lau,[1] Meron Tesfaye,[1,2] Claire R. Arthurs,[1,4,*] Isvar Cordova,[3] Cheng Wang,[3] Michael Yandrasits,[5,] and Ahmet Kusoglu[1,**,z]**

[1]*Energy Conversion Group, Lawrence Berkeley National Laboratory (LBNL), Berkeley, California 94720, United States of America*
[2]*Department of Chemical and Biomolecular Engineering, University of California, Berkeley, California 94720, United States of America*
[3]*Advanced Light Source, Lawrence Berkeley National Laboratory (LBNL), Berkeley, California 94720, United States of America*
[4]*Department of Mechanical Engineering, University of California, Berkeley, California 94720, United States of America*
[5]*3M Company, St. Paul, Minnesota 55144, United States of America*

Polymer-electrolyte membranes (PEMs) are a key component in electrochemical energy conversion devices where their main function is to selectively transport ionic species. Reducing PEM thickness is an effective strategy for improving performance by minimizing transport losses. However, how thickness affects the intrinsic properties of a membrane remains unexplored. This work aims to understand the effect of membrane thickness on structure-property relationships of 3 M perfluorosulfonic acid (PFSA) ionomer. We carried out a systematic investigation of membranes in a thickness range of 5–70 μm to examine their hydration behavior, morphology, crystallinity, mechanical properties, and gas and proton transport, with a discussion on the effect of thermal treatments. The collected dataset demonstrates PFSA membranes exhibit transitions in certain structural features below 10 μm, accompanied by an increased anisotropy in swelling and conductivity. Many properties deviate within 10%–20% without monotonic changes with thickness, however, linear correlations are observed between thickness and thermal-mechanical properties and gas permeability, although the latter is less significant. Identifying the thickness-dependence of PFSA properties could help expand the parameter window of PEMs, thereby enabling their optimization for automotive fuel cells, heavy-duty applications, and electrolyzers, especially if the membrane thickness is considered as part of dispersion-casting and reinforcement strategies.
© 2021 The Author(s). Published on behalf of The Electrochemical Society by IOP Publishing Limited. This is an open access article distributed under the terms of the Creative Commons Attribution Non-Commercial No Derivatives 4.0 License (CC BY-NC-ND, http://creativecommons.org/licenses/by-nc-nd/4.0/), which permits non-commercial reuse, distribution, and reproduction in any medium, provided the original work is not changed in any way and is properly cited. For permission for commercial reuse, please email: permissions@ioppublishing.org. [DOI: 10.1149/1945-7111/ac2973]

Manuscript submitted July 5, 2021; revised manuscript received August 17, 2021. Published October 22, 2021.

Supplementary material for this article is available online

Ion-conductive polymers are commonly used as the solid-electrolyte polymer membranes in electrochemical energy conversion devices, such as polymer-electrolyte fuel cells (PEFCs), electrolyzers, electrodialysis, and flow batteries.[1–7] In these devices, the thickness of the membrane has been observed to impact the cell performance, as thicker membranes often result in higher cell resistance and, consequently, lower cell conductance (i.e., inversely proportional to resistance). However, thinner membranes, while decreasing the area-specific resistance, also yield a larger crossover flux of reactants resulting in not only a low-power efficiency loss, but also a higher rate of degradation undermining the durability.[1,8–10] In addition, using thinner membranes is an effective way to reduce material costs, a favorable outcome for enabling commercialization of systems.[1,11] Thus, there exists a trade-off in terms of cost, performance and durability gains, optimization of which is essential for next-generation fuel-cell membranes. A recent analysis on fuel-cell membranes by General Motors researchers[1] demonstrated conductivity and permeability trade-off in a membrane of varying thickness directly impacts the durability and total cost of ownership. While any improvement in conductivity translates into increased power density and reduced stack cost, higher gas crossover (e.g., permeability) increases fuel cost and undermines membrane and system lifetime.[1]

Perfluorosulfonic acid (PFSA) ionomer is the preferred material for PEMs in PEFCs.[12] For several decades Nafion®, commercialized by the E.I. Dupont Co., has been the benchmark PFSA ionomer membrane for low–to-medium temperature PEFCs.[12–14] The widespread commercialization of PEFCs is however hindered by the poor performance of Nafion® at high temperature and low relative humidity conditions.[15–19] 3 M developed PFSAs of different equivalent weights (EWs) with a four-carbon side-chain, which exhibits a higher degree of crystallinity and glass transition temperature (T_g) for a given EW, and a higher proton conductivity at given RH.[20–25] Despite variations in side-chain chemistry and EW, however, most PFSA membranes exhibit unique interfacial phenomena, from surface morphology studies[26,27] to interfacial conductivity[27,28] and mass-transport studies for water.[10,29–32]

Membrane thickness has been demonstrated to affect cell performance. Zhao et al. studied the impact of Nafion (N11x) thickness on passive direct methanol fuel cells (DMFCs) and found that a thicker membrane (x = 174 μm vs 125 and 50 μm) exhibited higher fuel efficiency but the fuel cell performance varied with different operating conditions including methanol concentration and current density.[33] Another report by Seo et al. showed that thinner membrane Nafion NRE-212 (50 μm vs 127 and 183 μm) had improved DMFCs performance due to the reduction of proton transport resistance compared to thicker membranes.[34] Kim et al. also found that using a thicker membrane (Nafion 117, 175 μm) for a membrane electrode assembly (MEA) is the best method to reduce DMFC performance degradation under freeze-thaw cycles.[35] Jiang et al. studied the thickness of Nafion impact on the vanadium redox flow batteries.[6] Compared to 50 μm (Nafion 112), 88 μm (Nafion 1135) and 175 μm (Nafion 117), the 125 μm (Nafion 115) showed the highest energy efficiency and electrolyte utilization at a current density from 120–240 mA cm^{-2}. Recent simulation works indicated that membrane thickness is a crucial parameter influencing the performance of proton exchange membrane fuel cells (PEMFCs),[3] and PEM electrolyzers.[36]

Even though cell studies have demonstrated the effect of membrane thickness on performance, the question remains as to how the membrane's structure-functionality is affected by the thickness. Ex situ through-plane conductivity tests using membrane test system setup showed a thinner membrane (Nafion 111 vs Nafion

[a]Present address: Ballard Power Systems, 9000 Glenlyon Pkwy, Burnaby, BC, Canada.
*Electrochemical Society Student Member.
**Electrochemical Society Member.
[z]E-mail: akusoglu@lbl.gov

112, 1135, and 115) has higher proton conductivity.[28] However, relatively poor proton conductivity of the MEA based on the thinner membrane (Nafion 112, 50 μm) was found using in situ, current-interrupt measurements.[37] Computed X-ray microtomography and magnetic resonance imaging (MRI) were used to examine water distributions within Nafion membranes for an operating fuel cell,[38,39] and sorption kinetics were found to change with thickness.[39] Moreover, for Aciplex-S (Asahi Kasei) PFSAs, thinner membranes (56 μm) were found to have lower hydration than the thicker membranes (340 and 117 μm), although thinner membrane processing method could be different from the thicker ones.[38]

Thickness also impacts water transport through membranes.[18,19,21,23–25] Water transport through Nafion membranes using ex situ experimental techniques showed different transport rates on the interface and interior of the membrane when exposed to vapor.[27,29,32,39,40] These different transport rates were attributed to a hydrophobic skin layer (of a few hundred nm) on the membrane surface that impedes the water transport, even though this skin layer typically may not be observed in MEAs where the membrane contacts electrode layers with ionomers on each interface.[41,42] Nevertheless, the ex situ membrane surface's ionic conductance, which is believed to be directly related to the distribution of ionic clusters on the membrane surface, was found to change with the level of relative humidity using current-sensing atomic force microscopy.[27,43]

Light-duty and heavy-duty polymer electrolyte membrane fuel cells (PEFCs) require different performance and durability targets; achieving the latter might necessitate thicker or more stable membranes.[44,45] Thus, an improved understanding of the membrane functionality in the current and emerging applications of ionomers requires exploration of how thickness affects membrane properties. While the membranes used in the early studies were mostly extruded, newer generation PFSAs are solution-cast and exhibit different structures and properties.[46,47] In addition, even though there are studies on properties of Nafion at selected thicknesses as discussed previously, these are limited to the commercially available membranes (e.g., N211, 25 μm), and do not fully cover the thickness range relevant to the state-of-the-art fuel cell membranes (i.e., below 15 μm).[48] For example, Toyota Mirai uses a 14 micrometer-thick expanded polytetrafluoroethylene (ePTFE) reinforced PFSA membrane.[9,10,49] Similarly, recent studies by W.L. Gore and Associates reported properties of reinforced membranes as thin as 5 μm.[9,10,49,50] However, studieson the structure-property relationships, particularly the impact of thickness on nanostructure, thermal properties, gas transport properties of membranes, are sparse. Therefore, there is a need to investigate the impact of thickness on structure-property relationships of PFSA ionomers in a wider thickness range. To this end, the objective of this study is to investigate how the thickness of a dispersion-cast PFSA membrane impacts its structure and properties and identify the thickness regimes that can be exploited to improve and tune properties for various applications, including, but not limited to, PEFCs.

This study investigates the effect of thickness on proton-exchange membranes based on a 3 M PFSA chemistry. All membranes are used as non-reinforced, to decouple the impact of reinforcement and thickness-driven changes in structure-property correlations. Membrane structure and properties are measured as a function of thickness, in controlled environment. Moreover, swelling and conductivity of membrane are measured in two directions to examine thickness-driven anisotropy. The impact of relative humidity and temperature on the proton transport was also investigated for selected membrane thicknesses, to provide insights towards membrane design for high-temperature fuel-cell operation. Membrane nanostructure probed using a variety of X-ray scattering techniques was correlated with thermal-mechanical properties (using dynamic mechanical analysis) and mass transport properties (gas, water, and proton transport). The acquired data are analyzed to identify how thickness impacts properties and to provide insights on the extent to which thickness can be considered a design parameter for PEMs.

Experimental

Materials.—PFSA membranes were manufactured and provided by the 3 M Corporate Research Materials Lab (St. Paul, MN). The membranes were cast from 3 M 800 EW dispersion onto 50 μm-thick polyimide (Kapton) films with thicknesses of 70, 50, 20, 15, 10, 7.5, and 5 μm. However, titration of the membranes yield 820–825 g mol^{-1}, in line with 3 M PFSA membranes of the same chemistry investigated in other recent studies.[20,24,51] Membranes were cast on a pilot-scale coating line with four-zone drying ovens set to 45°, 75°, 135° and 145 °C. The membranes were then annealed in a separate process by contacting the liner side of the membrane to a roll heated to 200 °C for a total resentence time of 5 min. The thickness of the membranes was controlled by metering the casting solution through a precision slot-die during the roll-to-roll casting process. Additional thickness measurement of the membranes was carried out prior to measurements in the lab, as explained below. All the samples were used as-annealed with no further post-treatment. Selected membranes, however, were pretreated to provide a comparison with the annealed membranes. For the pre-treatment, membranes were heated in deionized (DI) water (Millipore, 18 MΩ) at 95 °C for 1 hr and stored in DI water prior to use. The temperature of the water was kept below 100 °C to avoid the agitation induced by the boiling process, which compromised the uniformity of the thinner membranes (<75 μm).

Thickness and swelling measurements.—The dimensional change of the membrane in liquid water with respect to its dry state, $\Delta A/A_{dry}$ and $\Delta L/L_{dry}$, were determined by measuring the change in diameter and thickness directions of a circular sample using Mitutoyo digital calipers and a Heidenhain-Metro 1200 depth measurement probe with ±0.2 μm accuracy, respectively. The system was retrofitted with a custom acrylic tip probe and measurement surface at room temperature. The membrane water volume fraction (Φ_w) was calculated as:

$$\Phi_w = \frac{\Delta V}{V_{wet}} = \frac{\Delta A \times \Delta L}{A_{wet} \times L_{wet}} \quad [1]$$

where ΔA and ΔL are the changes in cross-sectional area, and thickness of the equilibrated membrane in the wet and dry state, respectively. The thickness swelling ratio was calculated as $\Delta L_{wet}/L_{dry}$, and the in-plane swelling ratio was calculated as A_{wet}/A_{dry}. After soaking the membrane in liquid water for at least 3 days, samples were cut using a 0.25' circular die. Then the wet dimensions were obtained. The dry dimensions were taken after drying the sample overnight (12 h) in a container with anhydrous calcium desiccant, or by drying with dry N_2 feed for at least an hour at RT. Dimensions were calculated based on an average of 3 measurements.

Thermal gravimetric analysis (TGA).—The thermogravimetric analysis (TGA) was carried out using a Perkin Elmer TGA 4000 instrument equipped with an analytical balance and a controlled-atmosphere oven to measure a sample's mass loss as a function of temperature (from ambient *ca.* 25 °C to 800 °C) at a constant heating rate of 20 °C min^{-1} in nitrogen purge gas. The instrument had a sample temperature precision of ± 0.4 °C and a mass balance with an accuracy of ± 0.02%. For each test, a sample of 3–5 mg in weight was used. Between each test, careful cleaning was performed by holding the temperature at 900 °C for 10 min under the air atmosphere to oxidize all residue. The beginning of decomposition for each material was determined via the onset decomposition temperature, which was calculated by extrapolation of the TGA curve using the Perkin Elmer software.

Prior to heating, the sample was first dehydrated in ambient temperature using dry N_2 feed for at least 2 h to set the dry mass (M_0), after which the heating began. From this point forward, the mass loss with heating up to 120 °C ($\Delta M_{120\,^\circ C} = M_0 - M_{120\,^\circ C}$) was associated with the weakly-bound, residual water. The additional mass loss up to a temperature at which the rate of mass loss first reached zero was attributed to loss of the strongly-bound water. This occurred between 190 °C–220 °C for all samples. Mass loss, defined herein as positive, is converted to residual water content as follows:

$$\lambda_{\text{res}} = \frac{\Delta M_{120^\circ C}/18}{M_0/EW} \quad [2]$$

Water uptake and swelling.—Membrane water uptake as a function of relative humidity (RH) was measured with a dynamic vapor-sorption (DVS) analyzer (Surface Measurement Systems, UK) at 25 °C and 70 °C.[52,53] The samples were first dried at 25 °C, 0% RH for 2 h, in a consistent manner with the above-mentioned TGA procedure. Thereafter, the samples were humidified from 0 to 98% RH and then dehumidified from 98% to 0% with increments of 10% RH. Water uptake of the membrane, $\Delta M_w/M_0$, was continuously determined from the weight change (ΔM_w) with respect to the initial ("dry") weight, M_0, at 0% RH. At each RH step, the samples were equilibrated until the mass gain reached a steady-state ($dm/dt < 0.005\%\ \text{min}^{-1}$). The water content as a function of water activity, λ_{RH}, is calculated based on the water uptake, $\Delta M_w/M_0$ as:

$$\lambda_{RH}(RH) = \frac{mol(H_2O)}{mol(SO_3^-)} = \frac{\Delta M_W/18}{M_0/EW} \quad [3]$$

where EW is the equivalent weight of the membrane in g/mol, and 18 is the molecular weight of the water in g/mol. By definition, the above expression yields $\lambda = 0$, at 0%RH. To account for the non-zero, residual water at 0%RH, the total water uptake is expressed as (where the activity of water in vapor is $a_w = \text{RH}/100$):

$$\lambda(RH) = \lambda_{\text{res}}(0) + \lambda_{RH}(RH) \quad [4]$$

Dynamic mechanical analysis (DMA).—Mechanical properties of all membranes were studied in controlled strain amplitude mode using a dynamic mechanical analyzer (DMA) by TA Instruments Discovery DMA 850. The specimens with a width of 8 mm were placed at the tension clamp at the lock position. Dried house N_2 gas was fed through the DMA chamber overnight to remove all the ambient water and ensure a dry state for the polymer prior to the testing. The house N_2 gas was turned off before the experiment. The sample was strained between a fixed and a moving clamp in a static oscillation load. The specimens were tested at the frequency of 1.0 Hz, with 1 μm fixed-displacement amplitude, as cited at the ASTM standard (ASTM E1604–07) with a temperature sweep from room temperature to 150 °C at a ramping rate of 5 °C min^{-1}. From the collected stress-temperature data, storage modulus (E′), loss modulus (E′), and their ratio or tan(δ) were determined as a function of temperature.[54]

Gas permeability.—An in-house-built, constant-volume gas-permeator was used to measure gas permeability of the membranes, as described elsewhere.[55] It is also a completely dry system and therefore is suited for capturing intrinsic gas property of hygroscopic materials,[55] like PFSA. A membrane supported by a filter paper was sandwiched between two aluminum tape disks for mechanical stability and a well-defined area of gas transport flux. An active area diameter of 0.125–0.25 in. was used for samples. The prepared sample is placed in the permeation cell composed of a tightly sealed stainless-steel cross-flow cell between the downstream and upstream pressure transducers. The system is then degassed to remove any moisture and entrapped air with 5–12 h of exposure to vacuum prior to measurement. Initially, the downstream valve connecting the permeation cell to the vacuum pump is closed, and a slow pressure rise in the downstream volume is observed to monitor leak rate, recorded as a function of time ($\frac{dp_1}{dt}_{leak}$). The leak rate was maintained below 10% of the flux. Next, the feed gas was introduced to the upstream side of the membrane, and the pressure rise in the downstream volume was recorded as a function of time. Once a steady pressure rise in time is established, 10% of the last steady-state pressure rise ($\frac{dp_1}{dt}_{SS}$) is used to calculate permeability. For effectively constant pressure difference across the membrane, the downstream pressure was kept at 0.013 atm or less, while the upstream pressure was maintained at 1 atm or above. The temperature of the system was controlled using a constant-temperature water bath with a heater. All permeation experiments are performed at 35 °C. Membrane samples in this study were exposed to dry H_2 and O_2 gas (99.9% pure, Praxair, Danbury, CT) at the pressure of interest on the upstream side. The pressure range used in this study is 1 to 9 atm. Gas permeability (P_m) was calculated after subtracting the gas leak in the system using:

$$P_m = \frac{VL}{\Delta pART}\left(\frac{dp}{dt}_{SS} - \frac{dp_1}{dt}_{leak}\right) \quad [5]$$

where dp is the pressure gradient between upstream and downstream driving flux through the membrane. V is a known, enclosed, downstream volume where pressure rise associated with gas permeation is monitored, L is the membrane thickness, A is the active area, R and T are the gas constant, and experimental temperature of the water bath, respectively.

Contact angle.—Contact angle measurements of the as-received membranes were carried out using a goniometer (Rame-Hart) equipped with a two-camera system and a custom-made injection system, as described previously.[56] The water droplets were placed onto the membrane using a top injection method, and the liquid-water-droplet profile images were taken using a CCD capable of a frame rate of 60 Hz; droplets were backlit with a diffused 150 W halogen lamp. For each membrane, the measurements were repeated at least three times, and the contact angle values were calculated from the images recorded by both cameras using the DROPimage program. An average contact angle value with a standard deviation was determined.

Conductivity.—In-plane and through-plane conductivities of the specimens were both measured. The through-plane conductivity was measured using a Membrane Test System (MTS) (MTS740, Scribner Associates, Inc.). AC impedance measurements were performed under controlled humidity and temperature (ranged from 30 to 110 °C) with an SI 1260 impedance/gain-phase analyzer (Schlumberger Technologies, Inc.) and ZPlot software (Scribner Associates, Inc.), as described previously.[28] Membranes were cut into a rectangular piece with a dimension of 10 mm × 30 mm and were sandwiched between gas-diffusion electrodes (GDE) (IRD Fuel Cell Technology). The GDEs were attached to the platinum source electrode with conductive carbon paint, and then the membrane was compressed between the electrodes with a load of approximately 2.151 ± 0.017 MPa measured by a calibrated force spring and dial displacement indicator. Prior to testing, the samples were first kept at 70% RH and 30 °C under a nitrogen atmosphere for 2 h. Afterward, the samples were dehumidified to 20% RH with intervals of 10% RH, and then hydrated to 90% with an increment interval of 10% RH, then to 95% and 98% RH using a protocol similar to that used for the water-uptake measurements as described above. Samples were preconditioned for at least 30 min at each RH step, and then the membrane impedance was measured using voltage-controlled frequency sweep spectroscopy (10 mVAC at 0 VDC, 10 MHz to 1 Hz,

10 steps/decade).[28] The through-plane conductivity (κ) was calculated as:

$$\kappa = \frac{L}{RA} \quad [6]$$

where L is the average thickness of the membrane measured before and immediately after each test, R is the resistance derived from the intercept of the high-frequency impedance with the real axis, and A is the overlapping area of the platinum source electrodes (0.5 cm^2). For in-plane conductivity measurements, fully hydrated membranes were cut into 14.0 mm wide strips and placed in four-electrode BT-110 conductivity clamp (Scribner Associates). Prior to testing, the samples were kept in DI water for at least one hour to allow membrane equilibration. The in-plane conductivity was obtained using Eq. 5, where L is the distance between inner voltage electrodes (0.42 cm), R is the resistance of the membrane, and A is the cross-section area (Thickness × Width) of the membrane. Under vapor conditions, the dimensions of the membranes were measured using the same method as the through-plane conductivity. For liquid-water measurements, the measured sample dimensions in hydrated state are used.

Small- and wide-angle X-ray scattering (SAXS/WAXS).—Small/wide-angle X-ray scattering (SAXS/WAXS) experiments were performed in beamline 7.3.3 of the Advanced Light Source (ALS) at Lawrence Berkeley National Laboratory (LBNL). The X-ray wavelength used was $\lambda = 0.124$ nm, with a monochromator energy resolution of E/dE of 100, and the presented patterns were collected using a 2D Dectris Pilatus 2 M CCD detector (172 μm × 172 μm pixel size) at 25 °C. The scattering wave vector, $q = 4\pi \sin(\theta/2)/\lambda$, where θ is the scattering angle, was in the range of 0.001 to 0.04 $Å^{-1}$ for SAXS and 0.5 to 3 $Å^{-1}$ for WAXS. Experimental details can be found in previous studies.[57,58] For liquid-water equilibrated experiments, membranes were equilibrated in custom-designed solution cells with X-ray transparent Kapton™ windows for at least 12 h prior to imaging. The collected two-dimensional SAXS scattering patterns were azimuthally integrated to generate 1-D intensity profiles, I(q), which were corrected for background scattering. From the SAXS data, hydrophilic-domain spacing and inter-crystalline spacing, and full-width half-max (FWHM) were calculated using a Gaussian fit to the ionomer scattering peaks. WAXS images for vacuum-dried samples were obtained under ambient humidity (i.e., 35 to 40% RH). The relative degree of the crystallinity, x_c, is calculated from the relative integrated area of the crystalline and amorphous peak intensities, I_c and I_a, respectively, which are determined after the deconvolution of the WAXS peak using a double-Gaussian fit:[59]

$$x_c = \frac{\int q^2 I_c(q) dq}{\int q^2 I_c(q) dq + \int q^2 I_a(q) dq} \quad [7]$$

Tender resonant X-ray scattering (RXS).—Resonant X-ray Scattering (RXS) measurements across the "Tender" (~2–5 keV) X-ray energy regime were conducted in Japan's Photon Factory beamline 15 A-2, with a monochromator energy resolution of 2×10^{-4}.[60] Scattering data were collected using a Dectris PILATUS3 2 M CCD detector calibrated for low-energies and positioned 825 mm away from the sample. All dry samples were mounted as free-standing membranes on a metal plate that was loaded into a chamber which was held under vacuum (~10^{-3} T) at 25 °C. For measurements of wet samples, membranes were soaked in deionized (DI) water for at least 8 h prior to being cut into small (~1.5 mm^2) pieces so that they could be loaded into a vacuum-compatible flow cell (Protochips) custom-designed for in situ transmission-based X-

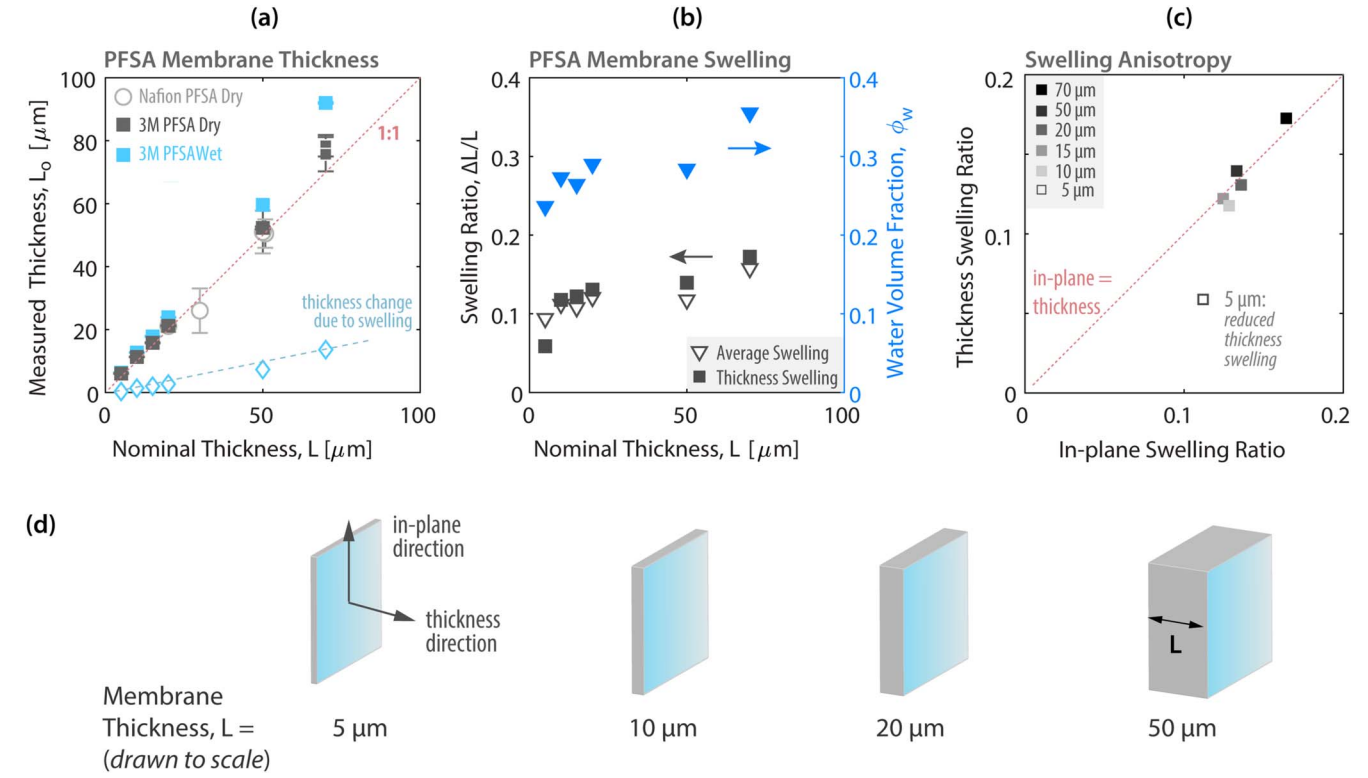

Figure 1. (a) Measured membrane thickness in dry and wet states against the nominal dry thickness provided by the manufacturer (set during the roll-to-roll processing). (b) Thickness swelling of the membrane ($\Delta L/L_0$) and water volume fraction measured from the thickness and area changes from dry to wet state. (c) Plot of thickness swelling vs in-plane swelling (determined from the area change, $\Delta A/A_0$) from dry to wet state. The wet state corresponds to equilibration in liquid water at RT. Each value is an average of three measurements. (d) Schematics of membrane thickness and directions. The error bars in (a,b) are included but comparable to marker size in some cases (*ca.* 3% standard deviation).

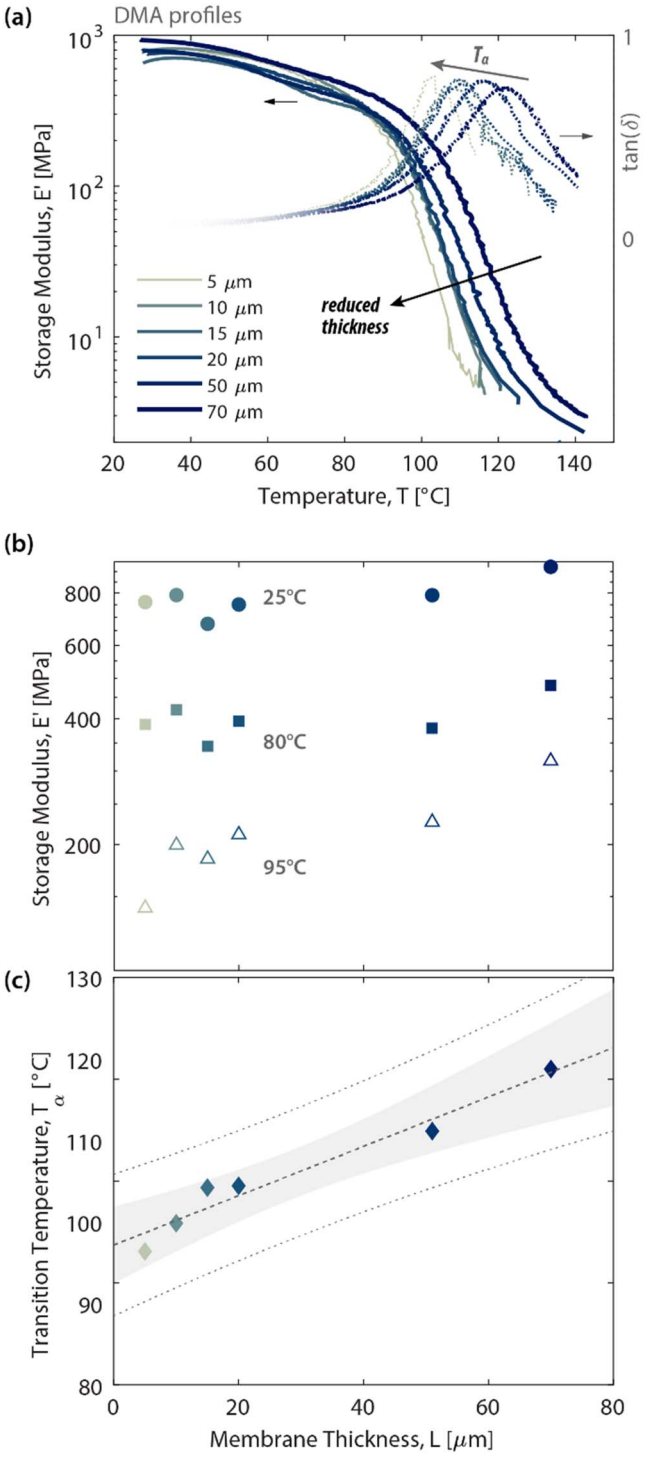

Figure 2. Temperature-dependent (a) storage moduli and tan(delta) of PFSA membranes measured with DMA. Effect of thickness on (b) Storage moduli at 25, 80, and 95 °C, and (c) alpha-transition temperature (from the peak of tan(delta)). In the plot c, the solid dashed line is the linear regression fit (correlation coefficient = 0.97), the gray shaded area represents the 95% confidence interval, and the dotted lines represent upper and lower prediction bounds.

ray measurements in the soft and tender energy range.[61,62] This cell encapsulated the pieces of membrane between two water-tight 50 nm-thick Si_3N_4 windows as deionized water was flowed through the cell at a rate of 300 μl h^{-1} with a programmable Harvard Apparatus Pump 11 Elite syringe pump. The X-ray energies chosen for these measurements ranged from 2460 eV (λ = 0.504 nm) to 2476 eV (λ = 0.500 nm) in order to enhance scattering contrast from ionomer domains, while avoiding the beam damage effects caused by measuring above the Sulfur K-edge whose X-ray absorption spectra has been reported for these 3 M materials.[61] The 2-D scattering patterns were azimuthally integrated and converted into 1-D intensity profiles, I(q), according to the incident X-ray energy used for each measurement.

Results

Membrane thickness and swelling.—Figure 1a compares the measured membrane thickness in both dry and wet states. The figure shows good agreement between the measured dry thickness and the nominal (manufacturer's) thickness, but only after drying in N_2 was employed. All membranes swell in water; an interesting observation is that their relative change w.r.t. dry thickness (i.e., swelling strain) is also higher for thicker membranes. This reveals a thickness-dependent swelling strain in PFSA membranes. Moreover, thickness swelling and the water volume fraction both decrease with reduced nominal thickness, although by preserving an almost isotropic swelling (Fig. 1b). Interestingly, once thickness reaches 5 μm, not only does membrane swelling begin to deviate from the thicker ones, but it also begins to exhibit swelling anisotropy: membrane swells less in the thickness direction, compared to that in-plane (Fig. 1c). These results indicate that the path towards thinner membranes, especially those with reinforcement for automotive applications, requires consideration of deviations in swelling compared to thicker dispersion-cast membranes.

Dynamic mechanical analysis.—Thermal-mechanical properties of membranes were measured using dynamic mechanical analysis (DMA) in controlled strain mode. Figure 2 shows the variation in storage modulus (E') and α-transition temperature with membrane thickness. As shown in Fig. 2b, decreasing membrane thickness in this range reduces its E' by 10% at 30 °C. The variation in E′ with thickness exceeds ±10% at temperatures 80 °C and higher. The α-transition temperature (T_α), so-called, ionic-network transition temperature, determined from the peak of tan(δ)-T curves is in the range of 100 to 120 °C (Fig. 2c), which is similar to previously reported values for Nafion and other 3M PFSA membranes.[12,63] Upon reducing the membrane thickness from 70 to 5 μm, T_α decreases linearly from 122 to 103 °C, indicating an enhanced polymer chain mobility in thinner membranes. A similar reduction in T_α has also been observed in the solution cast 3 M PFSA membrane when reducing EW from 1100 to 800 g mol^{-1} as measured by DMA.[23] A possible reason for such thickness-driven change in T_α. (for the same EW) could be as a result of the competition between the surface and internal forces governing the behavior of polymer aggregates, which could be influenced also by the casting process.

Thermal gravimetric analysis.—The thermal-gravimetric analysis (TGA) of PFSAs has been reported in many studies, some with coupled TGA-mass spectroscopy (TGA-MS) to identify the decomposition products.[64–70] Figure 3a depicts the TGA profiles and total water content loss during the first stage of the decomposition of PFSA membranes of selected thicknesses. Overall, all the membranes exhibit similar dehydration profiles (from 25 to 220 °C), followed by the onset of thermal decomposition around 390–405 °C and continuation of the degradation up to 520 °C, similar to the previous reports on Nafion.[12] The TGA profiles indicate the range of mass loss, defined as temperature range between initial and final decomposition ($\Delta T = T_i - T_e$), increases from 120 to 128 °C with a reduction in membrane thickness from 70 to 5 μm. The temperature at which the rate of mass loss first reached zero (i.e., 190–220 °C) can be attributed to the loss of all the water in the membrane, including the last water molecule in the primary hydration shell of the sulfonic acid groups (Fig. 3b).

Similarly, the water loss at 120 °C represents the strongly-bound water in the secondary hydration shells and is attributed to the

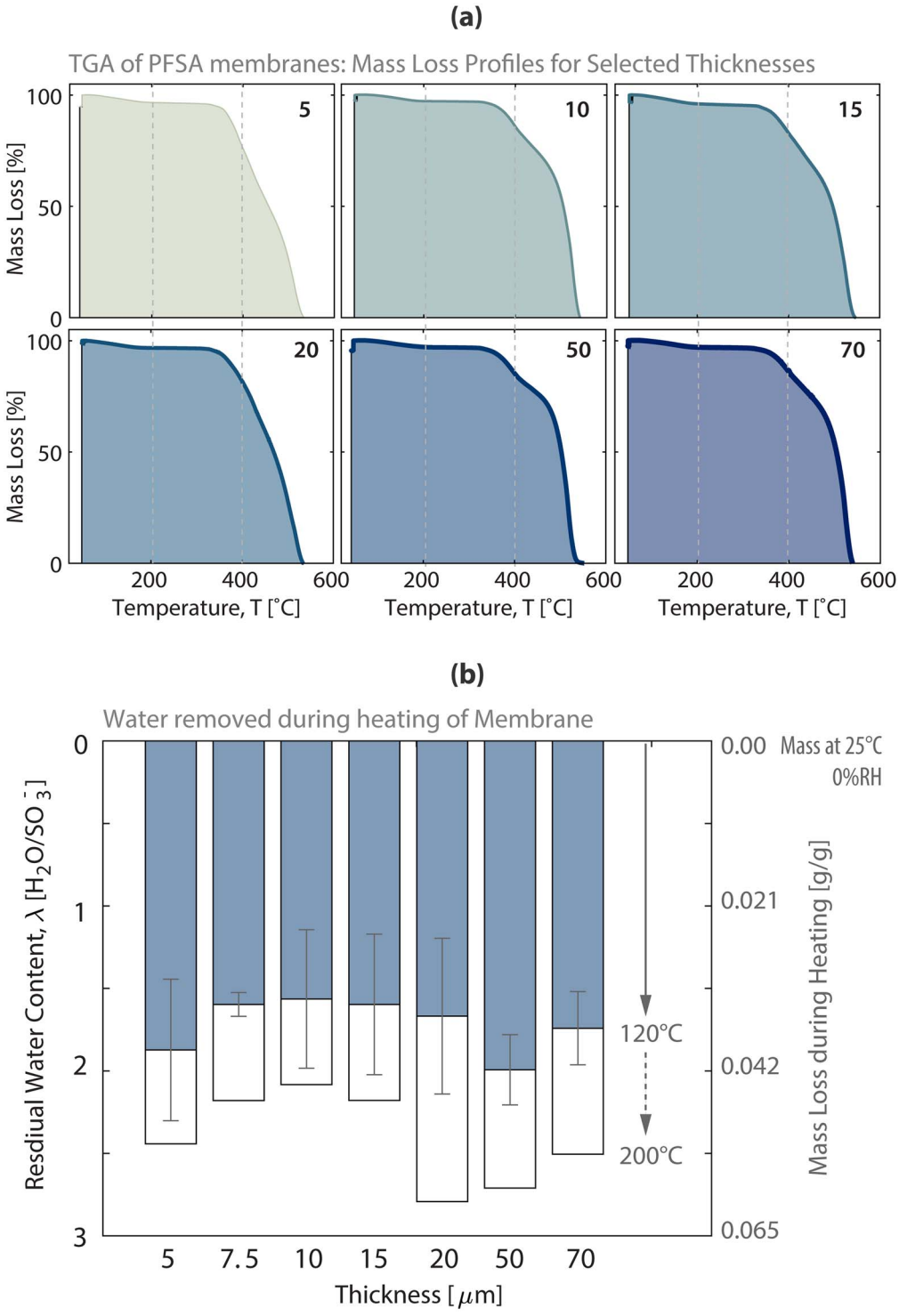

Figure 3. (a) Mass-Temperature TGA profiles of PFSA membranes at different thicknesses. (b) Effect of thickness on residual water in PFSA membrane at 0% RH associated with (and determined from) the dehydration of strongly-bound water upon heating from 25 to 120 °C and 200 °C, respectively. Higher loss of mass with heating indicates more "residual" water retained in the membrane at 25 °C, 0% RH.

"residual water," λ_{res}, which does not change significantly with thickness. In the remainder of this work, λ_{res} will be used as the bound water retained in the membrane at 0% RH. This is because the temperature of 200 °C required to remove the last water molecule removed in a TGA is higher than T_α (100 °C–120 °C) and therefore beyond a point of practical interest, including for fuel-cell operation.

Gas permeability.—The measured oxygen and hydrogen permeability values of the membranes are plotted as a function of membrane thickness in Fig. 4. Dry gas permeability through the membrane does not exhibit any thickness dependence down to 10 μm. To illustrate better the relative change in membrane's gas permeability, membrane's selectivity of H_2 over O_2, $S_{H_2} = P_{H_2}/P_{O_2}$ is used as a proxy for membrane's resistance to gas crossover (Fig. S1 available online at stacks.iop.org/JES/168/104517/mmedia), which shows only a slight increase below 5 μm thickness. For example, the (Pearson) correlation coefficient $\rho(P_{O_2}, L) = -0.12$, indicates a weak correlation. When H_2/O_2 selectivity is used as a

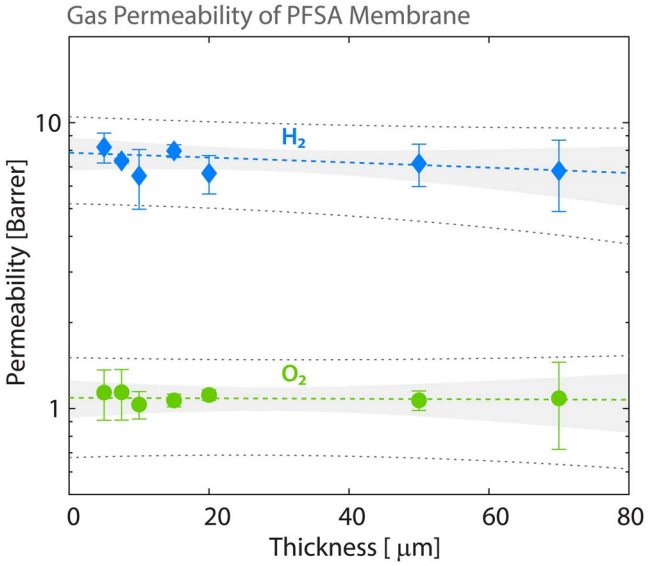

Figure 4. Permeability of O_2 and H_2 gases in a dry PFSA membrane plotted as a function of thickness. The dashed lines are the best-fit linear regression with the correlation coefficients of −0.37 and −0.12 for H_2 and O_2, respectively, which indicates weak dependence on thickness. The gray shaded area represents the 95% confidence interval, and the dotted lines represent upper and lower prediction bounds.

proxy to a barrier to H_2 permeability,[71] results reveal a lack of a strong thickness-driven change in selectivity as the membrane gets thinner (Fig. S1). Nevertheless, such changes could be amplified by the environment, especially at higher humidity and temperatures, which warrants further examination.

Water uptake behavior.—Membrane's water uptake behavior is characterized using sorption isotherms which depict in terms of water content (λ) as a function of relative humidity (RH) at constant temperature (Fig. 5). Sorption isotherms show comparable water-uptake profiles with a steep increase beyond 70% RH, which indicates the sorption of "free" water molecules in hydrophilic domains, in contrast to the low-RH regime where water molecules are within close proximity of the ionic groups.[12] The extent to which this nonlinearity is observed depends on the thickness. Both 70 μm and 50 μm membranes exhibit similar profiles to the 20 μm membrane. The sorption behavior of thinner membranes, however, deviates from this trend with more free water uptake close to saturation, except the thinnest membrane (5 μm) for which, water profile becomes less non-linear. Thus, maximum water uptake capacity close to saturation (98% RH) exhibits a non-monotonic dependence on thickness, as shown in Fig. 6a. This thickness-dependent trend exhibits less deviation for 80% and 50% RH. For lower RH values, however, water content remains comparable in thinner membranes, as they retain residual water (Fig. 3). In addition, as shown in Fig. S2, the contact angle also (θ_c) begins to decrease slightly for membranes below 10 μm, indicating a small increase in surface wettability.

Taken together, results indicate that membrane thickness affects hydration especially in high-RH regimes, where the key changes appear to be related to the nonlinearity of the uptake curve. Figure 6b shows the sorption isotherm created by the thickness-averaged water uptake of membranes with a larger statistical variation above 80% RH. A noteworthy consequence of these results is that the thinnest membrane (5 μm) exhibits less change in water content ($\Delta\lambda$) in response to RH variation could be an indicator of improved hydration stability that can be attained in next-generation PEMs. Such changes in water uptake in thinner membranes could be beneficial for creating ways to tune the water-retention capacity of membranes for low-RH or high-temperature conditions, and could be altered further in the presence of stabilizers and reinforcements.

Nanostructure.—WAXS data for the membranes do not show any discernable change in crystallinity with the thickness (Fig. S4), with a relative degree of crystallinity values of 8.9%–11%. This is consistent with the lack of a significant deviation in mechanical properties, as well as in gas permeation.

SAXS profiles of membranes are summarized in Figs. 7a–7c, which show the characteristic features of PFSA ionomers with (i) an ionomer peak ($q = 0.1$–0.2 Å^{-1}) corresponding to phase-separation, and (ii) a matrix knee ($q = 0.02$–0.08 Å^{-1}) associated with the inter-crystalline correlation within the hydrophobic matrix of nano-morphology.[51] Figure 7c shows that, based on SAXS profiles acquired at 10 keV (hard X-ray), both peaks exhibit only slight variation with membrane thickness in the hydrated (wet) state. The position of the ionomer peak arising from correlation length between the hydrophilic nano-domains can be used to determine the domain spacing, d. In the hydrated state, d-spacing is within a range of 4.1 ± 0.1 nm for 15–70 μm (Fig. 7b). These membranes also possess a similar full-width half-max (FWHM), a measure of peak broadness and an indicator for the degree of phase-separation.[51,52,72] (Fig. 7b) However, as can be seen in Fig. 7c, the SAXS profile for 5 μm deviates from these trends with a broader ionomer peak. This would indicate a weaker phase separation and an increased disorder of domain-network. Nevertheless, this could also be arising from the reduced X-ray contrast in a thinner membrane. Because, as membranes become thinner than 20 μm, their X-ray cross-sections at hard energies decrease (see SI, Fig. S3), making it difficult to detect scattering signals from these same characteristic peaks. Therefore, a SAXS beamline with access to X-rays in the tender energy regime was used to extract better than the aforementioned ionomer domain information from these thinner films.

Specifically, tender X-ray energies near the *Sulfur K-edge* (~2460–2490 eV) improved the sensitivity of scattering contrast to ionomer domains compared to what could be achieved with hard X-rays due to their higher cross-sections for thinner membranes (as indicated by the differences in transmission shown in Fig. S3) as well as contrast-enhancement effects due to resonance with the sulfur-containing ionomer domains.[61] This resulted in distinctly pronounced scattering features compared to standard hard X-ray SAXS (10 keV), as shown in Figs. 7a–7b for 5 and 7.5 μm membranes. Such signal enhancement on resonance (at Sulfur K-edge) is even stronger in the dry state, when the scattering contrast is typically much weaker due to lack of water that reduces the electron density differences between the hydrophilic and hydrophobic domains. For this reason, the SAXS spectra for the dry membranes are shown only in the low eV regime, a comparison with hard X-rays is shown in Fig. 7b for a wet membrane. The results show a significantly improved X-ray signal as evidenced by the well-defined ionomer peak, in both dry and wet states. These spectra also allow for the determination of d-spacing with greater precision. In a dry membrane, d-spacing decreases from 2.9 nm to 2.65 nm when the membrane thickness is reduced from 70 to 5 μm. While seemingly a small change, the fact that the dry d-spacing decreases monotonically indicates a thickness-dependent trend. In addition, these values are of interest for modeling the cluster morphology of ionomers in a dry state.[12,73,74] In the hydrated state, however, d-spacing is higher for thinner membranes (<5 μm), which would yield a thickness-dependent nano-swelling response as will be analyzed later in the discussion section. Similarly, the FWHM of the ionomer peak also decreases for thinner membranes as can been inferred from their more well-defined ionomer peaks (Figs. 7a–7b). The nanostructural changes in thinner membranes could be related to two phenomena:

(1) Reduced disorder in domain-network, implying slightly less tortuous transport pathways in the ionomer once its thickness approaches a few micrometers. The fact that thin membranes

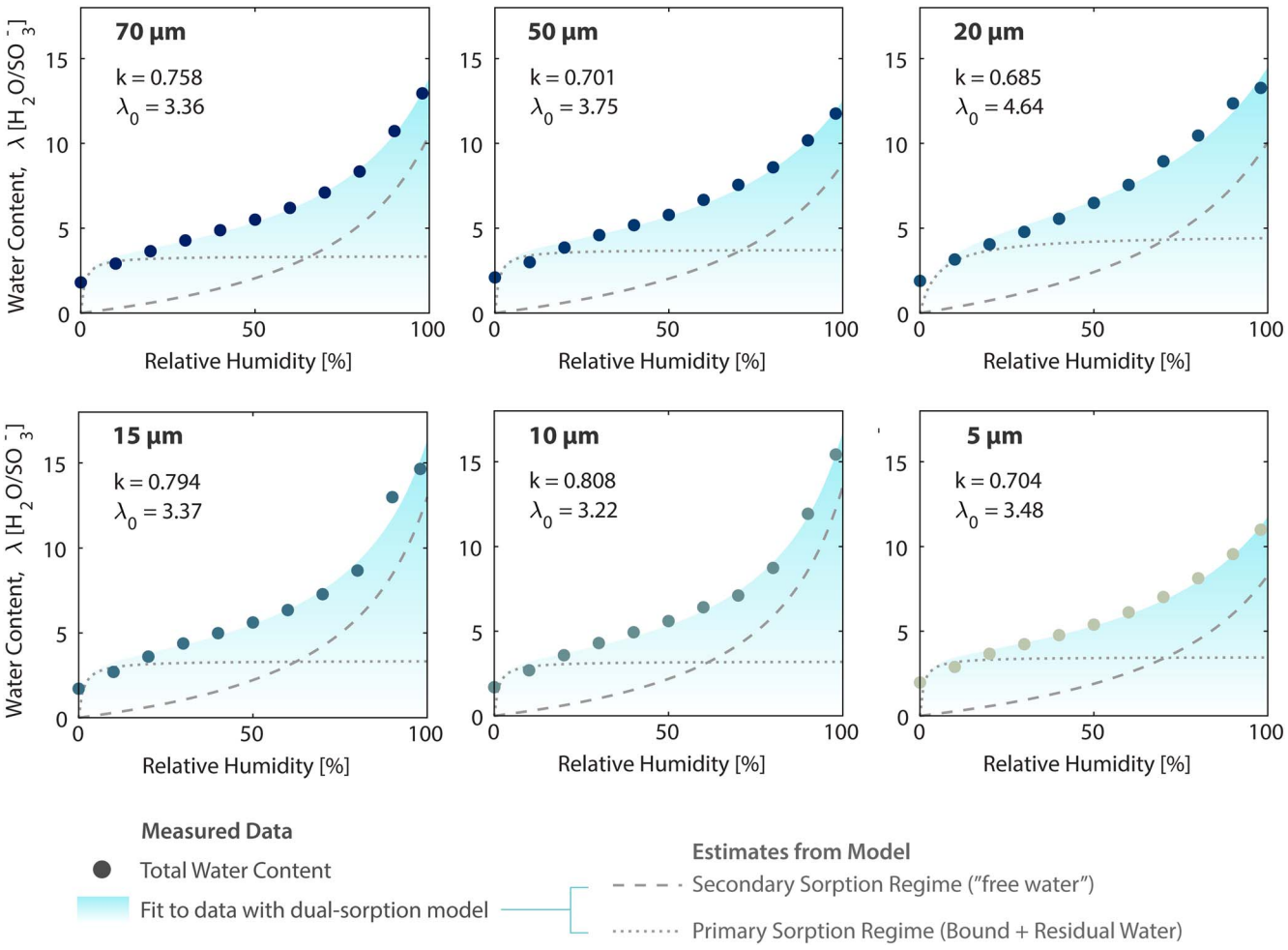

Figure 5. Sorption isotherms of PFSA membrane at 25 °C in terms of water content as a function of RH (circles). The shaded region represents the data reproduced by dual-sorption model (as shown in Eq. 8), which is used to deconvolute the sorption isotherm into two regimes of hydration: (i) dotted lines, primary sorption regime (bound water + residual water), and (ii) dashed lines, secondary sorption regime. The k and λ_0 are the model parameters used to generate the model curves. The higher k values in thinner membranes reflect nonlinearity of the sorption curve, meaning a more steep increase in λ with RH close to saturation.

exhibit a well-defined shape even in a dry state could be explained by a more stable domain-network formed during fabrication.

(2) Since these changes are captured only with tender X-ray energies near the Sulfur K-edge, the improved sensitivity to ionomer domains in thinner membranes can be due to scattering contrast effects. In this scenario, reduced thickness does not just change the structure, but also creates a better effective "sample volume" for X-ray scattering measurements, resulting in a stronger peak signal.

Interestingly, previous studies showed that ionomer films of 50–250 nm thickness cast on a $Si(O_2)$ substrate exhibit changes in their phase-separation usually with a reduced d-spacing, compared to 20 μm membranes.[75,72] While these sub-micron results are consistent with our first proposed phenomenon and seem to support the notion that similar effects may begin to manifest themselves as membrane thickness approaches micron level, the second phenomenon still cannot be ruled out as a contributing factor.

It can be inferred from this dataset change in morphology of ionomer from bulk (thick membranes) to thin spun-cast films could indeed be a continuous trend that begins to manifest itself strongly around the sub-micron thickness range.

Ion conductivity.—Ion conductivity of membranes measured in two directions, in-plane vs thickness, are summarized in Figure 8. Conductivity in the through-plane direction, $\kappa_\perp$, begins to exhibit a strong thickness dependence below 15 μm. However, compared to the changes in $\kappa_\perp$, the conductivity in the plane, $\kappa_\parallel$, shows minor change with thickness, for both 70% and 95% RH. These results indicate that conductivity begins to deviate from isotropy especially for thinner membranes (<15 μm). Anisotropic conductivity was typically observed in extruded membranes induced by different orientations from extrusion direction and through-plane direction of the fabrication process.[47] Solution-cast PFSA membranes usually exhibit negligible anisotropic conductivity.[76] However, in the current study, the differences in conductivity between the in-plane and thickness (through-plane) directions are noteworthy (over 20% difference at low RH), especially below 15 µm. We used the anisotropy factor (ξ_κ) to quantify the anisotropy ratio in conductivity, calculated as follows:.

$$\xi_\kappa = \frac{\kappa_\parallel - \kappa_\perp}{\kappa_\parallel + \kappa_\perp} \qquad [8]$$

When conductivity is the same in two directions, $\xi_\kappa = 0$, (isotropy), whereas a for a hypothetical membrane that conducts only in the plane ($\kappa_\perp \to 0$), $\xi_\kappa \to 1$. For thicker membranes, the anisotropy ratio is close to $\xi_\kappa = 0$ (isotropy); but ξ_κ increases as the membrane gets thinner. For 5 and 10 μm-membranes, ξ_κ approaches 0.1 at 95% RH, and 0.15 at 70% RH (Fig. 8). The results indicate conductivity

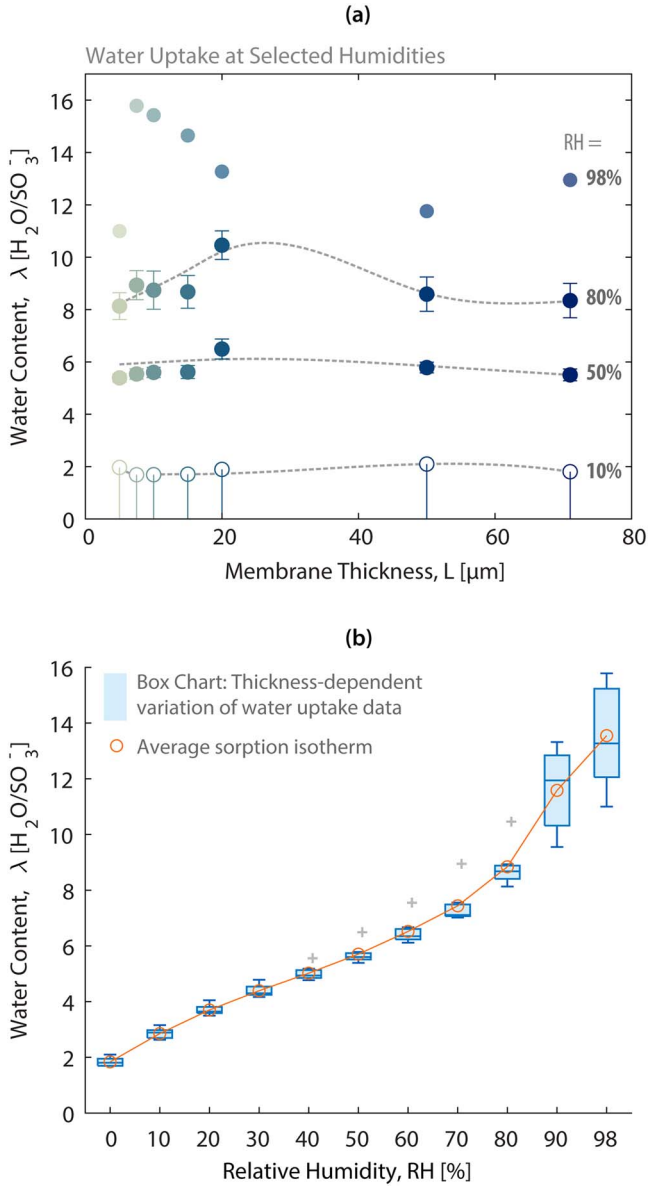

Figure 6. Effect of thickness on hydration in terms of the number of water molecules per mole of the ionic group. (a) Water content at different membranes thicknesses for selected RH values. All the values include residual water measured at 0% RH. Dashed gray lines are spline fits to serve as a guide-to-the-eye. (b) Box and whisker chart representing the statistical variation of the water content due to membrane thickness change at each RH (the thickness values are the same as shown in (a)). The circle-line shows the average values, and + symbol represents the outliers.

begins to exhibit a slight anisotropy for membranes thinner than 10 μm. For example, at higher RH, through-plane conductivity decreases more than 10% compared to in-plane conductivity for the 5 μm membrane, whereas membranes within the 20–70 μm range exhibit comparable conductivity in both directions (Fig. 8). The reason could be due to the more pronounced interfacial effects as the membrane gets thinner, even though it must be noted that these interfacial effects on resistance measurements may be less pronounced or altered with further processing or conditioning of MEAs, making this effect possibly less of an issue in fuel cells..[10,27,41,77]

To examine the hydration-conductivity relationship of these membranes,[12] the measured RH-dependent in-plane conductivity (κ) is plotted in Fig. 9 as a function of water volume fraction (Φ_w). The slope of this conductivity-hydration relationship remains unchanged up to $\Phi_w = 0.15$, and then changes with the thickness (Fig. 9). Usually, such a change in κ—Φ_w (or λ) relationship occurs due to changes in thermal history (e.g., pretreatment) or membrane chemistry (e.g., EW).[12,20,52,72,73,78–81] Notably, our results indicate that the conductivity-hydration relationship could change even for the membranes with the same chemistry and thermal history, and in fact, conductivity at given hydration level shows a non-monotonic thickness dependence: it first decreases and then increases for thinner membranes (5 μm). (Figure 9) An interesting outcome of this trend is that conductivity might increase more than water uptake does for certain membrane thicknesses (Fig. 6), hinting a way to modify ion-water transport functionality due possibly to changes in tortuosity,[12,82,83] higher polymer chain mobility (Fig. 2), surface hydrophilicity (Fig. S2) and nano-domain network (Fig. 7).

Increasing the cell operating temperature is considered one of the effective solutions to mitigate the problems that cause poor cell performance.[84] The United States Department of Energy (DOE) has established 120 °C as the temperature target for the year 2020–2025 for automotive applications.[85] To examine high-temperature properties, the proton conductivity is measured at 30 °C–110 °C for selected membranes. The correlation of conductivity and temperature, exhibits Arrhenius-type behavior for all membrane thicknesses, as is shown in Fig. 10. The activation energies (E_a) are obtained using $\left(\kappa = \mathrm{B}\, exp\left(-\frac{Ea}{RT}\right)\right)$, where R is the gas constant (8.314 J mol^{-1} K^{-1}); B is a prefactor, and T is the temperature (K). An interesting finding is that E_a does not exhibit an apparent dependence on thickness: it increases for 10 μm and then decreases for 5 μm.

Discussion

Even though the membranes studied herein possess the same chemistry and thermal history; they show thickness dependence for several properties. Below 10 μm, membranes begin to exhibit dramatic changes in structure and properties, including reduced thermal-transition temperature and storage modulus, and improved conductivity at a given hydration level. The reason for such dramatic changes could be governed by a combination of factors, which will be examined further below. To assist with the discussion, the changes in selected properties are analyzed and tabulated in Table I and Fig. 11. For many of the properties, the change with thickness was within ±10%, and without clear monotonic trends, especially for water uptaken and conductivity, which were also conflated with their RH dependence. This must be noted in the evaluation of thickness-driven changes in permeability and thermal-mechanical properties, which are reported in the dry state. The 5 μm membrane showed a decrease in properties such as thermal-transition, water uptake, swelling, and conductivity (compared to average). The most significant changes (> 25%) between the thinnest and thickest membranes are observed for properties measured in the thickness direction, namely swelling and conductivity.

Morphological factors.—A key phenomenon governing PFSA membrane properties is the nano-swelling of hydrophilic water domains in a phase-separated domain network. Using the d-spacing values for dry and wet membranes (Fig. 7), nano-swelling of the membrane is found to increase with decreasing thickness (Fig. 12). Considering a possibly stronger degree of phase-separation in thinner membranes (Fig. 7f), increased nano-swelling indicates changes in both domain-network and local structure of hydrophilic domains. Such effects could explain the underlying morphological origins of the observed changes in transport properties, in particular, the enhanced in-plane conductivity below 10 μm even at the same hydration level (Fig. 9). If thinner membranes could accommodate water molecules in a less tortuous domain network, this could explain the reduced resistance to ion transport and increase in the slope of κ—Φ_w in the hydrated state.

Table I. Summary of membrane thickness effect on structure and properties. Relative change in each property with respect to its average overall thicknesses is summarized and defined as negligible (within ±5% change, or within the experimental error in some cases), low (within ±15% change), and high (more than ±20% change). T-Rex indicates scattering with tender X-rays.

Property	Trend: As thickness reduces from 70 to 5 μm	Degree of Impact	Notes
Hydration and Structure			
Contact Angle	Decreases	Low	Ambient
Low-RH water-uptake ($<$ 30% RH)	Does not change	Negligible	vapor, at 25 °C
High-RH water uptake ($<$ 80% RH)	Non-monotonic	High	vapor, at 25 °C
Domain spacing (wet)	Increases	Low	SAXS, T-Rex (in water)
Domain spacing (dry)	Decreases	Low	SAXS (dry)
Degree of phase-separation (wet)	Increases ($<$ 7.5 μm)	Low	SAXS, T-Rex (in water)
In-plane swelling in water	Decreases	Low	in water, at 25 °C
Thickness swelling in water	Decreases ($<$ 5 μm)	High	in water, at 25 °C
Thermal-Mechanical Stability			
Crystallinity	Does not change	Negligible	WAXS
T-decomposition range	Increases	Low	TGA (220–500 °C)
Storage Modulus	Decreases	Low	DMA (dry)
α-transition temperature	Decreases	Low	DMA (dry)
Gas Transport			
O_2 Permeability	Does not change	Negligible	dry
H_2 Permeability	Increases	Low	dry
Ion Transport			
In-plane conductivity	Decreases	Low	vapor
Thickness conductivity	Decreases ($<$ 10 μm)	Low	vapor
Conductivity Anisotropy = In-plane/Thickness Conductivity	Increases ($<$ 10 μm)	High	High impact at low RH
Area-Specific resistance	Decreases	High	vapor
Activation Energy	Non-monotonic	Low	vapor (25–80 °C)

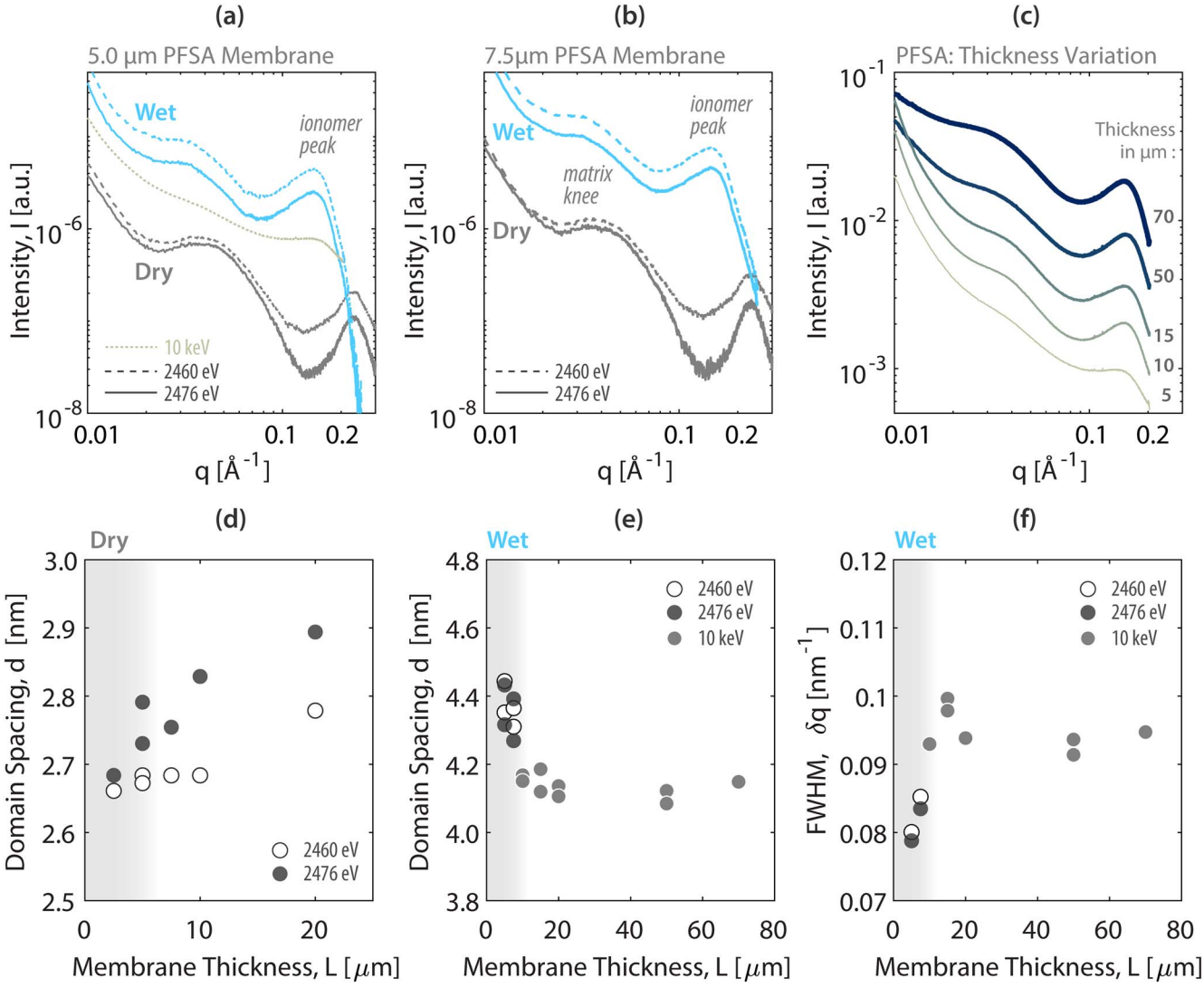

Figure 7. SAXS profiles for (a) 5 and (b) 7.5 μm PFSA membrane in dry and wet states collected with Tender X-rays at 2460 eV and 2476 eV (Sulfur K-edge). (c) Effect of thickness on SAXS profiles at 10 keV (hard X-rays) for membranes with 5 thicknesses. The profile for 5 μm (10 keV) is also shown in (a) to show the increased contrast accessed with the Tender X-ray energies. Domain spacing of the hydrophilic domains determined from the ionomer-peak positions in the (d) dry and (e) wet states. (f) shows the full-width half max (FWHM) of the ionomer peak in the wet state. In (d-f), the shaded regions indicate the thickness range where the signal-to-noise ratio was enhanced with Tender X-rays. Open, filled, grey symbols, are obtained at 2460 eV, 2476 eV, and 10 keV, respectively.

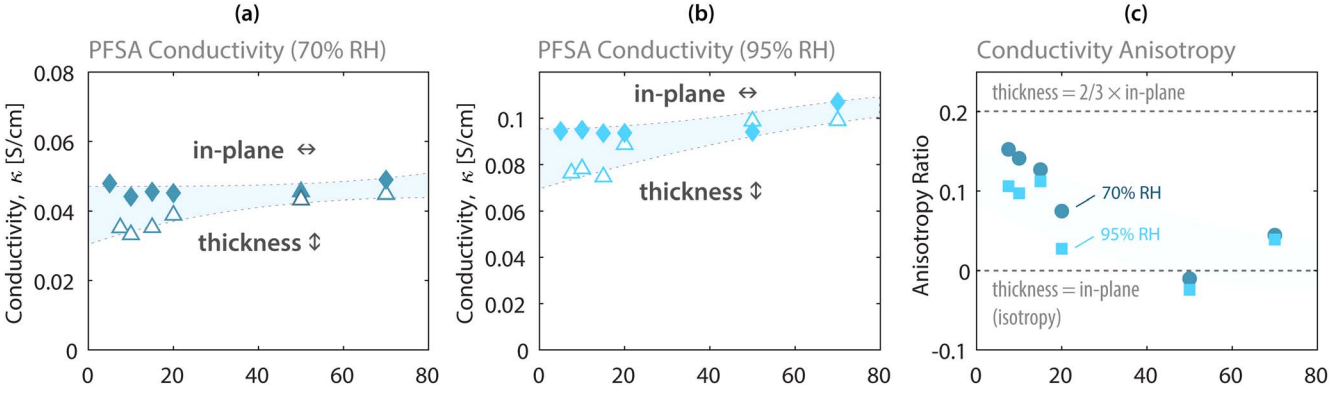

Figure 8. Effect of thickness on in-plane vs thickness conductivity at (a) 70 and (b) 95% RH, at 30 °C. (c) Anisotropy for conductivity begins to increase as the membrane thickness decreases below 20 μm. (See text for the explanation). The dashed lines in (c) indicate the calculated values for the cases of an isotropic membrane (thickness and in-plane conductivity are the same), and an anisotropic membrane for which thickness conductivity is 50% of the in-plane conductivity.

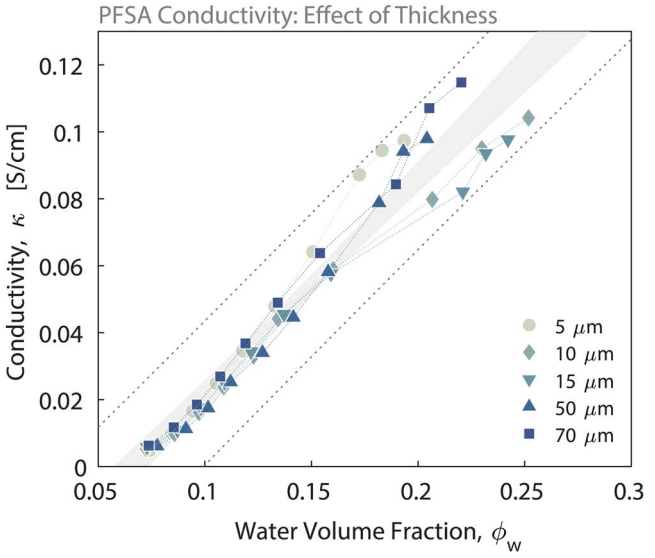

Figure 9. In-plane proton conductivity of 3 M PFSA (825 EW) membrane as a function of water volume fraction for selected thicknesses (lighter colors indicate lower thickness). The gray shaded area represents the 95% confidence interval, and the dotted lines represent upper and lower prediction bounds, based on the combined dataset for five thickness values. Water volume fraction is determined from the water uptake data (Fig. 5), all the values are measured at RT.

Analysis of sorption isotherms.—To analyze the sorption isotherms and quantify the effect of thickness, the water uptake is fitted using a modified version of the dual-mode sorption model, which combines two distinct modes of sorption; the Langmuir-type (1st bracket) and free (2nd bracket) sorption:[73,86]

$$\lambda(a_w) = \left\{\bar{\lambda}_0 \frac{(S-1)ka_w}{1+(S-1)ka_w}\right\} + \left\{\bar{\lambda}_0 \frac{ka_w}{1-ka_w}\right\} \qquad [9]$$

In the context of this model, $\overline{\lambda_0}$ corresponds to the water molecules that reside within the hydration layer of ionic sites and remain bound to them. Parameters k and S, represent, respectively, the interaction between the water molecules and the ionomer moieties, and that between the water molecules within the adjacent adsorption layers. As seen from Fig. 5, the model can reproduce the experimental data fairly well using the set of best-fit parameters (listed in Table SII and shown in Fig. 5). The chosen model is relatively simplistic in form, compared to more advanced models that can account for additional interactions and chemical-mechanical properties,[52,74] but since the chemistry of the membrane and its ionic interactions are not changing, the expression suffices to reproduce the measured data and allow for quantification of the thickness-driven changes in the nonlinearity of the uptake curves.

Factors controlling an ionomer's sorption behavior can be summed up under physical-chemical and mechanical-structural factors.[12,52,73] Physical-chemical interactions can be represented by $\overline{\lambda_p}$, which is related to the residual water in the primary hydration shell as discussed above (Fig. 3b). Since the ionomer chemical identity does not vary, any change in this low-RH regime can be attributed to the membrane's water-retention capacity (λ_{res}). The parameter, k, which reflects the degree of the upturn at higher water activity, changes with thickness. The higher k values in thinner membranes reflect the nonlinearity of the sorption curve with a more steep increase in λ with RH close to saturation.

Change in swelling could be attributed to mechanical and structural factors: (i) increased ionomer matrix stiffness opposing swelling (thereby shifting uptake curve down), (ii) ionomer network's reduced structural flexibility to accommodate water adsorption at high RH. The mechanical factor (i) could be tied to the modulus of the ionomer in the dry state, which decreases as the membrane gets thinner (from 70 to 10 μm) (Fig. 2), albeit slightly, thereby reducing the forces opposing swelling and shifting the uptake curve upwards. Nevertheless, this mechanical factor cannot alone explain the reduced water content and for the thinnest membranes (5 μm), which, exhibit a higher nano-swelling inferred from SAXS (Fig. 12). The origin of discrepancy might lie in the structural changes; reduced disorder in local structure could make the membrane accommodate water molecules more efficiently. One would expect such a membrane to have a relatively higher conductivity for a given hydration level due to a less tortuous transport pathway within local domains. This is indeed the case for the thinnest membrane, as shown in Fig. 9. Despite the small variations in these properties with thickness, their correlation nevertheless supports the structure-property relationships observed in PFSA membranes. Overall, the key impact of the thickness on high-RH hydration of PFSA membranes appears to be the nonlinearity of the uptake curve. A practical consequence of such behavior is that the relative change in water uptake with RH, $\Delta\lambda/\Delta a_w$, depends on the thickness and attains a lower value for the 5 μm membrane, which could be associated with hydration response and stability of fuel-cell membranes in vapor.

Processing and pretreatment effects.—Thermal treatments such as boiling in acid, hydrogen peroxide, and water strongly impact the properties, morphology, and performance of the PFSA

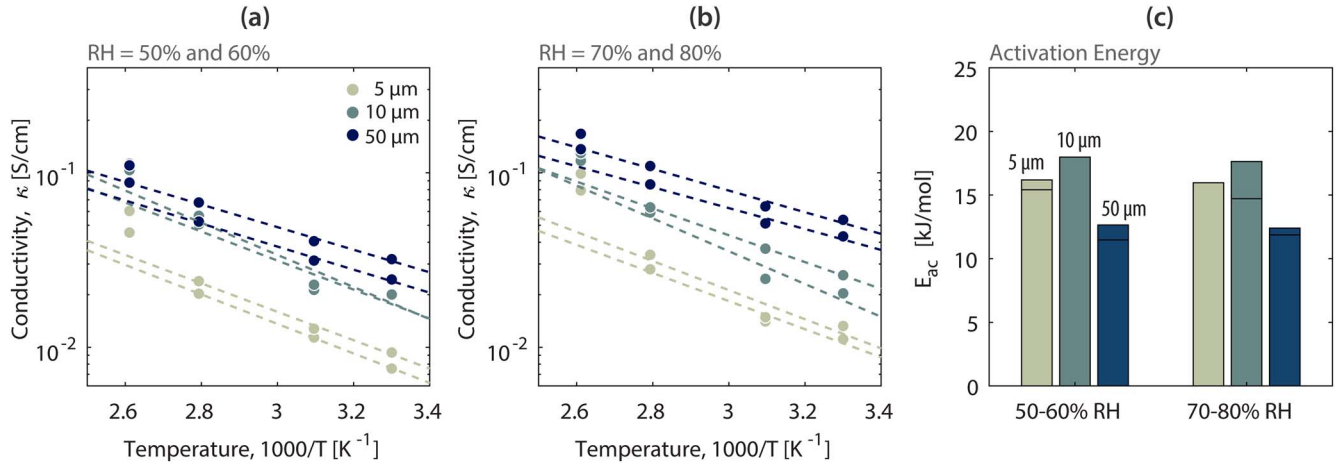

Figure 10. Effect of thickness on conductivity (in the thickness direction) shown as in terms of Arrhenius plots of (log) conductivity at different RH levels: (a) 50% and 60% RH (higher values), and (b) 70% and 80% RH (higher values). (c) The activation energy for conductivity for the data in a-b, where the lines represent the lower and higher RH values. (Dark to lighter colors indicate reduced thickness in all plots).

Figure 11. Change in properties (P) of PFSA membrane of varying thickness (L) visualized in terms of the deviation of a property for each membrane thickness, P_L, from the average of the properties over six thicknesses, P_{ave}. (Average of the membrane thicknesses is L_{ave} = 28 μm). The average (P_{ave}) and standard deviation (δP) for each property is tabulated on the right, along with representative values for the 20 μm-thick membrane values ($P_{L=20}$). Additional information on trends and experimental conditions are also provided in Table I.

membranes.[12,52,79,83,87–95] While the membranes studied herein are used in the annealed form (*i.e.*, "as-received"), it is of interest to examine the effect of boiling on annealed membranes. Figure 13a shows the comparison of in-plane conductivity of 3 M PFSA membranes in annealed and pre-boiled form. As expected, pre-boiled membranes exhibit higher conductivity, which could be attributed to higher water uptake as a result of post-processing.[37,52,79,90,94,96] This is evidenced by an increased hydrophilic domain-spacing upon boiling, regardless of the membrane thickness (Fig. 13b). A striking finding, however, membrane thickness also alters the relative change in conductivity incurred due to boiling. Pre-boiling causes a larger increase in conductivity for thinner membranes, while it results in a minimum change for the thickest 50 μm membrane (Fig. 13a). Nevertheless, boiling-induced increase in water d-spacing does vary with the thickness (Fig. 13b). This discrepancy can be resolved upon examination of the inter-crystalline peak (matrix knee) for boiled and annealed membranes (Fig. 13c). The matrix knee for 70 μm membrane does not appear to change with thermal history (*e.g.*, boiling). For thinner membranes, however, pre-boiling reduces the intensity of the matrix knee, unraveling morphological changes in the matrix in favor of a reduced inter-crystalline network, which could explain the enhanced conductivity. Thus, the interplay between pretreatment and thickness appears to be more a result of domain-network alterations than it is a consequence of local changes.

It was previously shown that annealed membranes have lower water uptake, slower diffusion, and more disordered nanostructure, which allude to an inter-connected domain network that is partially collapsed and kinetically trapped.[12,52,79,97–100] Boiling the membrane in water enables this structure to reach a new quasi-equilibrium state with an expanded and better-connected network, thereby increasing the hydration capacity and conductivity, as shown in Fig. 13. It is suggested that proton channels near the membrane surface reorient from perpendicular to parallel to the surface as the annealing temperature approaches the membrane's transition temperature (T_α).[98] In our study, T_α is a function of the membrane thickness but the annealing temperature was constant (T_{ann} = 200 °C). This results in a thermal driving force, $\Delta T_a = T_{ann} - T_\alpha(L)$, which increases as the membrane gets thinner. A 10x decrease in membrane

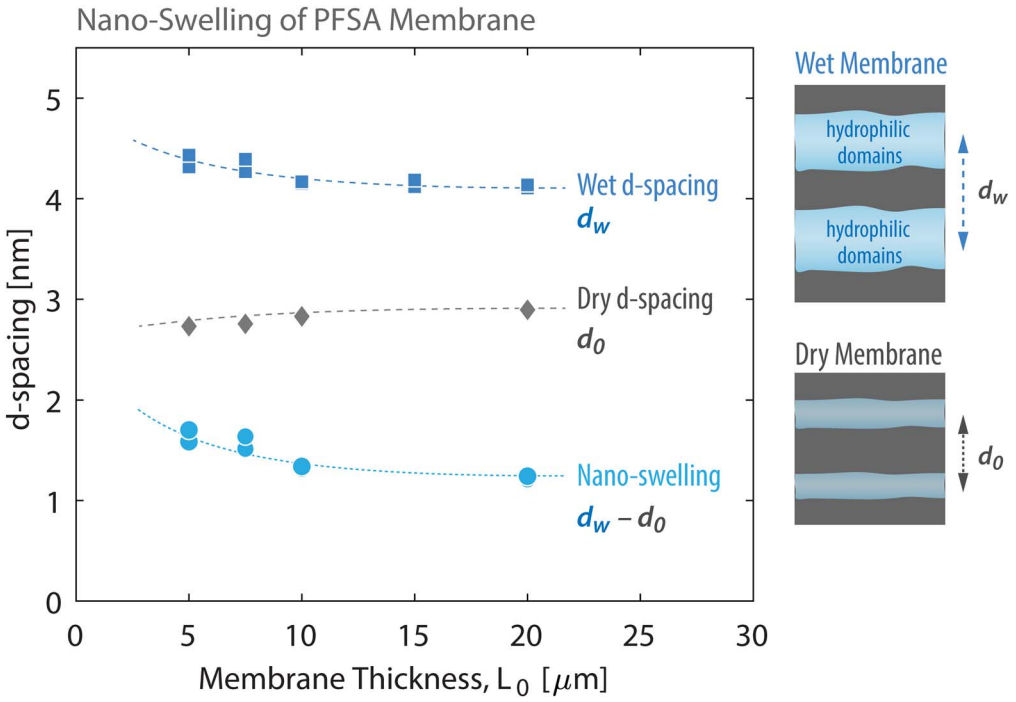

Figure 12. Effect of thickness on domain spacing of membrane in dry and wet state, as well as their difference, namely, the nano-swelling determined from SAXS studies shown in Fig. 7. Spline curves are guide-for-the-eye.

thickness (from 50 to 5 μm) increases ΔT_a from 78 °C to 97 °C during annealing, the impact of which on the rearrangement of polymer chains is probably conflated with the solvent effects. During a typical casting process, thicker membranes are expected to dry slower as a result of a larger volume of solvent being evaporated. However, the membranes in this work were dried in a four-zone drying oven that slowly ramps the temperature during solvent evaporation, and then annealed separately. Also, the membranes were cast on a 50 μm liner acting as a heat sink which alleviates the thickness effect from a heat transfer perspective. Moreover, the crystallinity of the annealed membranes does not reveal a strong trend with the thickness (Fig. S4). Therefore, the observed changes in T_α could be less affected by the solvent and drying/quenching effects, but perhaps related to the surface constraints imposed by the liner and/or air surface restricting the chain motion and the domain-network in thinner PEMs. This restricted network then becomes more responsive to post-treatment in water, thereby causing a higher increase in conductivity upon boiling (Fig. 13). In contrast, the 70 μm PEM exhibits a relatively smaller difference in structure-conductivity properties between annealed and boiled forms. Hence, the thickness of a PFSA membrane could affect its properties, and also their change with post-treatment, yet the coupled nature of surface and annealing effects must be considered when establishing correlations between morphology and fabrication methods.

The evolution of ionomer structure during casting and annealing processes might change with thickness and drying conditions, rendering interfacial effects more dominant in thinner membranes.[29,32,95,101] Interestingly, such effects are even more pronounced in ionomers cast as nanometer-thick thin-films on supports.[95,101–103] Tesfaye et al. showed that substrated-supported dispersion cast 3 M and Nafion ionomer thin films (20–400 nm thickness) exhibit a thickness-dependent thermal transition, T_α, which decreases within the sub-micron regime due to free-surface effects, but then increases due to the restricted mobility of ionomer domains imposed by the substrate.[104] Thus, one cannot rule out the role of the free-surface effects on membrane response during casting, which could likely change with thickness, and contribute to the changes in T_α, as observed in this work.

In addition, a recent study by Berlinger et al.[95] showed casting affects properties differently when an ionomer is cast as a thin-film vs a micron-thick bulk membrane. As such, pretreatment such as pre-boiling could help thinner membranes reach structural equilibrium and consequently alter their transport property. A similar phenomenon was previously observed for membranes undergone heat treatment studies.[87,45] These findings suggest that processing effects and thickness could be intertwined during the manufacturing of dispersion-cast membranes even for the same ionomer chemistry. These indicators are critical not only for optimizing PEMs for fuel-cells,[44] but the changes in membrane properties with water treatment could also be beneficial for water electrolyzers and redox flow batteries, where membranes are usually operated in hydrated conditions.

Summary and outlook.—The impact of thickness on the structure, hydration, thermal-mechanical, and ion and gas transport properties of membranes are investigated and the key trends are summarized in Table I. The collected data unraveled a set of thickness-dependent changes in certain membrane properties, while some properties remained invariant to thickness. These trends enable us to identify the transition regimes within 5–15 micrometers for the properties investigated herein. Key observations are summarized as follows:

- Membranes exhibit isotropic swelling (in-plane vs thickness) from 70 to 7.5 μm, below which a reduced swelling occurs in the thickness direction.
- Conductivity in the plane of the membrane does not change with thickness. Conductivity in the thickness direction, however, begins to decrease below 15 μm compared to in-plane. This thickness-driven anisotropy causes a 10%-20% deviation in conductivity of thinner membranes measured in the plane vs thickness directions (depending on the RH).
- Some structural features of thinner membranes cannot be resolved with hard (>10 keV) X-ray scattering due to low contrast, but this can be improved using X-rays with energies near the sulfur atom's absorption K-edge. Results from SAXS in this "tender" energy range unraveled reduced domain spacing in the dry state for thinner membranes and a slightly improved degree of nano-phase separation.
- Thermal-transition temperature, T_α, and storage moduli decrease monotonically with reduced membrane thickness, which

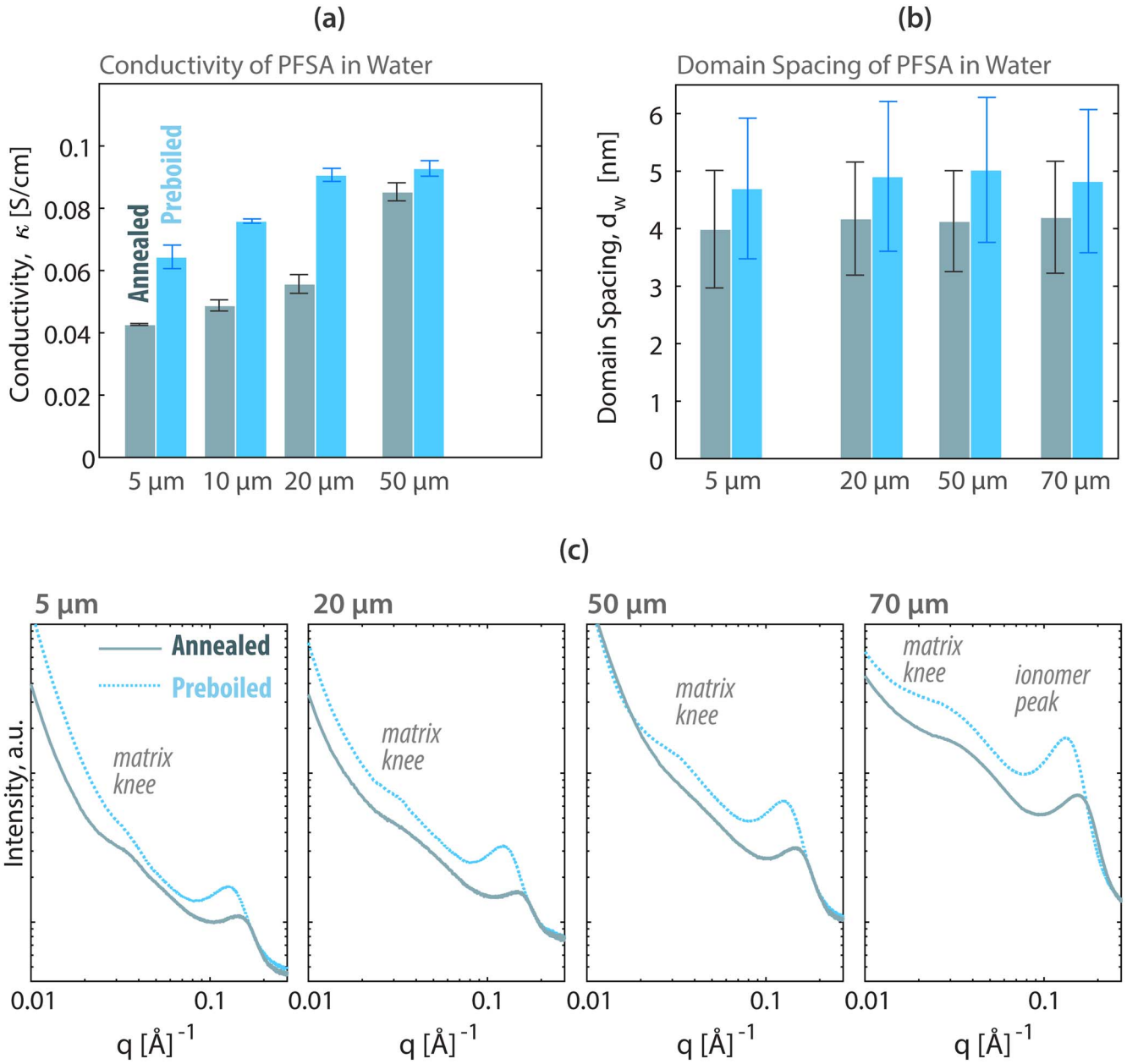

Figure 13. The impact of as-annealed (dark) and preboiling (light) in water on (a) In-plane (DC) proton conductivity PFSA membrane b) Domain spacing of PFSA membrane measured in liquid water at 25 °C (c) SAXS profiles of PFSA of different thickness.

could be intertwined with the morphological changes that had incurred during annealing

- Changes in crystallinity, oxygen, and hydrogen gas permeability with thickness are within ±10%. Given the significant changes in RH-dependent water uptake with thickness, gas transport properties might change more at higher humidities or temperatures, or in the presence of additives and reinforcements.
- It is plausible that thickness changes the interplay between the internal (bulk) and interfacial (surface) structure of membranes and their relative impact on properties.

In addition, in characterizing PEMs, one should be cognizant of the following issues:

- The emergence of anisotropy and orientation-dependence in properties (below 10 μm).
- Limitations of the bulk-membrane techniques with signal-to-noise issues for membranes thinner than 5 μm.
- The PFSA membrane thickness in a dry state can approach the manufacturers' nominal thickness only after the membrane is dried in 0% RH using an inert (e.g., N_2) gas. This was shown to be the case regardless of the membrane thickness.
- The residual water remained in membranes even after drying (at 0% RH) which could affect the measured properties in "dry" state. Those strongly-bound water molecules could be removed (or determined) only by heating the membrane between 100 to 200 °C. Mass losses measured by TGA and DVS matched when a consistent drying procedure (e.g. dry N_2 flow for 1–2 h) is adopted to set the reference mass at 0% RH.
- Conductivity calculations in the hydrated state should account for the dimensional changes and anisotropy which become especially important for determining accurate ASR values (see Fig. S5 for an example).
- The ability of low-energy X-ray techniques to resolve features especially in thinner membranes (< 7.5 μm) that can otherwise not be deciphered using traditional hard X-ray techniques due to reduced transmission and scattering contrast.

Conclusions

This study investigates how thickness affects the structure and properties of proton-exchange membranes by using a medium-side chain (3 M) PFSA ionomer dispersion-cast to a range of thicknesses (5 to 70 μm). The swelling and conductivity of the membrane are measured in two directions, which showed thickness-driven deviation from isotropy below 10 μm. Our findings reveal that membranes dispersion-cast thinner than 10 μm exhibit changes in certain properties, which could be as a result of pronounced interfacial effects or morphological changes imposed during casting and annealing. These observed changes occurred for the membranes of the same chemistry and thermal history highlight the role thickness could play in ionomer properties, with implications for controlling PEM performance further through casting and processing effects. The reported thickness-property map could provide new insights for examining performance and stability trade-offs, help with the reinforcement strategies relying on thinner ionomer layers, and guide the design and development of separator-electrolyte membranes for applications such as heavy-duty fuel cells or electrolyzers.

Acknowledgments

The authors would like to thank Thomas Chan and Dr. Douglas Kushner for assisting with experimental work, and Drs. Andrew Crothers, and Adam Weber for insightful discussions and helpful comments. This work was supported by the Fuel-Cell Performance and Durability (FC-PAD) and MillionMile Fuel Cell Truck (M2FCT) consortium (https://millionmilefuelcelltruck.org), technology manager Greg Kleen, which is supported by the U.S. Department of Energy (DOE), Office of Energy Efficiency and Renewable Energy, Hydrogen and Fuel Cell Technologies Office (HFTO), under contract no. DE-AC02-05CH11231. We thank Chenhui Zhu and Eric Schaible for their assistance with facilitating the equipment at the Advanced Light Source (ALS) beamline 7.3.3, supported by the Office of Science, Office of Basic Energy Sciences, of the U.S. DOE (Contract No. DE-AC02-05CH11231). AK would like to acknowledge the ECS-Toyota Fellowship and thank Paul Fanson and Hongfei Jia of Toyota for helpful discussions.

ORCID

Michael Yandrasits https://orcid.org/0000-0002-9493-0588
Ahmet Kusoglu https://orcid.org/0000-0002-2761-1050

References

1. C. S. Gittleman, A. Kongkanand, D. Masten, and W. B. Gu, *Current Opinion in Electrochemistry*, **18**, 81 (2019).
2. W. Xin, Z. Zhang, X. Huang, Y. Hu, T. Zhou, C. Zhu, X.-Y. Kong, L. Jiang, and L. Wen, *Nat. Commun.*, **10**, 3876 (2019).
3. R. K. S. S. Vuppala, B. A. Chedir, L. Jiang, L. Chen, M. Aziz, and A. P. Sasmito, *Molecules*, **24**, 3097 (2019).
4. J. Renner, K. Ayers, and E. Anderson, *PEM Electrolysis for Hydrogen Production: Principles and Applications* (CRC Press, New York, NY) (2015).
5. D. Chen, M. A. Hickner, E. Agar, and E. C. Kumbur, *J. Membr. Sci.*, **437**, 108 (2013).
6. B. Jiang, L. Wu, L. Yu, X. Qiu, and J. Xi, *J. Membr. Sci.*, **510**, 18 (2016).
7. K. Jiao and X. Li, *Prog. Energy Combust. Sci.*, **37**, 221 (2011).
8. S. J. Hamrock and A. M. Herring, *Encyclopedia of Sustainability Science and Technology*, ed. R. Meyers (Springer, New York, NY) 8328 (2012).
9. W. Liu, T. Suzuki, H. Mao, and T. Schmiedel, *ECS Trans.*, **50**, 51 (2013).
10. E. L. Redmond, K. U. Hansen, and D. W. Berg, *ECS Trans.*, **92**, 445 (2019).
11. C. Zhang, *Nat. Energy*, **4**, 89 (2019).
12. A. Kusoglu and A. Z. Weber, *Chem. Rev.*, **117**, 987 (2017).
13. K. A. Mauritz and R. B. Moore, *Chem. Rev.*, **104**, 4535 (2004).
14. X. Luo, S. Holdcroft, A. Mani, Y. Zhang, and Z. Shi, *Phys. Chem. Chem. Phys.* (2011).
15. T. J. Peckham and S. Holdcroft, *Adv. Mater.*, **22**, 4660 (2010).
16. T. J. Peckham, J. Schmeisser, M. Rodgers, and S. Holdcroft, *J. Mater. Chem.*, **17**, 3255 (2007).
17. A. Mani and S. Holdcroft, *J. Electroanal. Chem.*, **651**, 211 (2011).
18. S. Bose, T. Kuila, T. X. H. Nguyen, N. H. Kim, K.-T. Lau, and J. H. Lee, *Prog. Polym. Sci.*, **36**, 813 (2011).
19. R. E. Rosli, A. B. Sulong, W. R. W. Daud, M. A. Zulkifley, T. Husaini, M. I. Rosli, E. H. Majlan, and M. A. Haque, *Int. J. Hydrogen Energy*, **42**, 9293 (2017).
20. A. Kusoglu et al., *Chem. Mater.*, **32**, 38 (2020).
21. J. M. Larson, S. J. Hamrock, G. M. Haugen, P. Pham, W. M. Lamanna, and A. B. Moss, *J. Power Sources*, **172**, 108 (2007).
22. M. Maalouf, C. N. Sun, B. Pyle, M. Emery, G. M. Haugen, S. J. Hamrock, and T. A. Zawodzinski, *Int. J. Hydrogen Energy*, **39**, 2795 (2014).
23. M. S. Schaberg, J. E. Abulu, G. M. Haugen, M. A. Emery, S. J. O'Conner, P. N. Xiong, and S. Hamrock, *ECS Trans.*, **33**, 627 (2010).
24. M. Yandrasits, M. Lindell, M. Schaberg, and M. Kurkowski, *The Electrochemical Society Interface*, **26**, 49 (2017).
25. S.-H. Shin, P. J. Nur, A. Kodir, D.-H. Kwak, H. Lee, D. Shin, and B. Bae, *ACS Omega*, **4**, 19153 (2019).
26. N. J. Economou, A. M. Barnes, A. J. Wheat, M. S. Schaberg, S. J. Hamrock, and S. K. Buratto, *J. Phys. Chem. B*, **119**, 14280 (2015).
27. Q. He, A. Kusoglu, I. T. Lucas, K. Clark, A. Z. Weber, and R. Kostecki, *J. Phys. Chem. B*, **115**, 11650 (2011).
28. K. R. Cooper, *J. Electrochem. Soc.*, **157**, B1731 (2010).
29. B. Kienitz, H. Yamada, N. Nonoyama, and A. Z. Weber, *J. Fuel Cell Sci. Technol.*, **8**, 011013 (2011).
30. D. A. Caulk, A. M. Brenner, and S. M. Clapham, *J. Electrochem. Soc.*, **159**, F518 (2012).
31. M. B. Satterfield and J. B. Benziger, *J. Phys. Chem. B*, **112**, 3693 (2008).
32. X. Y. Luo and S. Holdcroft, *J. Membr. Sci.*, **520**, 155 (2016).
33. J. G. Liu, T. S. Zhao, Z. X. Liang, and R. Chen, *J. Power Sources*, **153**, 61 (2006).
34. S. H. Seo and C. S. Lee, *Proc. Inst. Mech. Eng. Part C J. Mech. Eng. Sci.*, **224**, 2211 (2010).
35. Y. Oh, S.-K. Kim, D.-H. Peck, D.-H. Jung, and Y. Shul, *Int. J. Hydrogen Energy*, **39**, 15760 (2014).
36. S. Toghyani, S. Sheikh Fakhradini, E. Afshari, E. Baniasadi, M. Jamalabadi, and M. S. Shadloo, *Int. J. Hydrogen Energy* (2019).
37. S. Slade, S. A. Campbell, T. R. Ralph, and F. C. Walsh, *J. Electrochem. Soc.*, **149**, A1556 (2002).
38. K. Teranishi, S. Tsushima, and S. Hirai, *Electrochem. Solid-State Lett.*, **8**, A281 (2005).
39. G. S. Hwang, D. Y. Parkinson, A. Kusoglu, A. A. MacDowell, and A. Z. Weber, *ACS Macro Lett.*, **2**, 288 (2013).
40. Q. Zhao, P. Majsztrik, and J. Benziger, *J. Phys. Chem. B*, **115**, 2717 (2011).
41. K. D. Kreuer, *Solid State Ionics*, **252**, 93 (2013).
42. R. Hiesgen, S. Helmly, T. Morawietz, X. Z. Yuan, H. J. Wang, and K. A. Friedrich, *Electrochim. Acta*, **110**, 292 (2013).
43. A. J. Steinbach and D. M. Peppin, *ECS Trans.*, **58**, 1589 (2013).
44. David A. Cullen, K. C. Neyerlin, Rajesh K. Ahluwalia, Rangachary Mukundan, Karren L. More, Rodney L. Borup, Adam Z. Weber, Deborah J. Myers, and Ahmet Kusoglu, "New roads and challenges for fuel cells in heavy-duty transportation." *Nature Energy*, **6**, 462–74 (2021).
45. W. Xie, R. M. Darling, and M. L. Perry, *J. Electrochem. Soc.*, **163**, A5084 (2015).
46. A. Mokrini, N. Raymond, K. Theberge, L. Robitaille, C. Del Rio, M. C. Ojeda, P. G. Escribano, and J. L. Acosta, *ECS Trans.*, **33**, 855 (2010).
47. K. Cooper, *ECS Trans.*, **41**, 1371 (2011).
48. T. Yoshida and K. Kojima, *The Electrochemical Society Interface*, **24**, 45 (2015).
49. E. L. Redmond, S. Wriston, and J. L. Szarka, *ECS Trans.*, **80**, 633 (2017).
50. M. Crum and W. Liu, *ECS Trans.*, **3**, 541 (2006).
51. G. M. Su, I. A. Cordova, M. A. Yandrasits, M. Lindell, J. Feng, C. Wang, and A. Kusoglu, *JACS*, **141**, 13547 (2019).
52. A. Kusoglu, S. Savagatrup, K. T. Clark, and A. Z. Weber, *Macromolecules*, **45**, 7467 (2012).
53. A. Kusoglu and A. Z. Weber, *Polymers for Energy Storage and Delivery: Polyelectrolytes for Batteries and Fuel Cells* (American Chemical Society, Washington, DC) 175 (2012).
54. K. P. Menard and N. Menard, *Encyclopedia of Analytical Chemistry*, 1 (2017).
55. S. M. Meckler, J. E. Bachman, B. P. Robertson, C. Zhu, J. R. Long, and B. A. Helms, *Angew. Chem. Int. Ed.*, **57**, 4912 (2018).
56. P. K. Das, A. Grippin, A. Kwong, and A. Z. Weber, *J. Electrochem. Soc.*, **159**, B489 (2012).
57. A. Kusoglu and A. Z. Weber, *ECS Trans.*, **50**, 961 (2013).
58. A. Kusoglu, K. T. Cho, R. A. Prato, and A. Z. Weber, *Solid State Ionics*, **252**, 68 (2013).
59. R. J. Roe, *Methods of X-ray and Neutron Scattering in Polymer Science* (Oxford University Press, Oxford) (2000).
60. N. Igarashi, H. Takagi, H. Ohta, T. Mori, S. Tomita, Y. Nagatani, T. Kosuge, H. Okuda, and N. Shimizu, *AIP Conf. Proc.*, **2054**, 060043 (2019).
61. G. M. Su, I. A. Cordova, M. A. Yandrasits, M. Lindell, J. Feng, C. Wang, and A. Kusoglu, *J. Am. Chem. Soc.*, **141**, 13547 (2019).
62. G. M. Su, I. A. Cordova, M. A. Brady, D. Prendergast, and C. Wang, *Polymer*, **99**, 782 (2016).
63. S. J. Osborn, M. K. Hassan, G. M. Divoux, D. W. Rhoades, K. A. Mauritz, and R. B. Moore, *Macromolecules*, **40**, 3886 (2007).
64. L. G. Lage, P. G. Delgado, and Y. Kawano, *J. Therm. Anal. Calorim.*, **75**, 521 (2004).
65. Y. Iwai and T. Yamanishi, *Polym. Degrad. Stab.*, **94**, 679 (2009).
66. C. Bas, N. D. Alberola, and L. Flandin, *J. Membr. Sci.*, **363**, 67 (2010).
67. E. Moukheiber, C. Bas, N. D. Alberola, and L. Flandin, *J. Membr. Sci.*, **431**, 105 (2013).
68. Y. F. Fan, D. Tongren, and C. J. Cornelius, *Eur. Polym. J.*, **50**, 271 (2014).
69. M. Feng, R. Qu, Z. Wei, L. Wang, P. Sun, and Z. Wang, *Sci. Rep.*, **5**, 9859 (2015).
70. T. Shimoaka, C. Wakai, T. Sakabe, S. Yamazaki, and T. Hasegawa, *Phys. Chem. Chem. Phys.*, **17**, 8843 (2015).

71. B. D. Freeman, *Macromolecules*, **32**, 375 (1999).
72. A. Kusoglu, T. J. Dursch, and A. Z. Weber, *Adv. Funct. Mater.*, **26**, 4961 (2016).
73. S. W. Shi, A. Z. Weber, and A. Kusoglu, *Electrochim. Acta*, **220**, 517 (2016).
74. A. R. Crothers, R. M. Darling, A. Kusoglu, C. J. Radke, and A. Z. Weber, *J. Electrochem. Soc.*, **167**, 013547 (2020).
75. A. Kusoglu, *Encyclopedia of Sustainability Science and Technology*, ed. R. A. Meyers (Springer, New York, NY) 1 (2018).
76. J. Peron, A. Mani, X. Zhao, D. Edwards, M. Adachi, T. Soboleva, Z. Shi, Z. Xie, T. Navessin, and S. Holdcroft, *J. Membr. Sci.*, **356**, 44 (2010).
77. X. Luo, A. Wright, T. Weissbach, and S. Holdcroft, *J. Power Sources*, **375**, 442 (2018).
78. S. W. Shi, A. Z. Weber, and A. Kusoglu, *J. Membr. Sci.*, **516**, 123 (2016).
79. S. W. Shi, T. J. Dursch, C. Blake, R. Mukundan, R. L. Borup, A. Z. Weber, and A. Kusoglu, *J. Polym. Sci., Part B: Polym. Phys.*, **54**, 570 (2016).
80. K. D. Kreuer, M. Schuster, B. Obliers, O. Diat, U. Traub, A. Fuchs, U. Klock, S. J. Paddison, and J. Maier, *J. Power Sources*, **178**, 499 (2008).
81. K. D. Kreuer and G. Portale, *Adv. Funct. Mater.*, **23**, 5390 (2013).
82. P. Choi, N. H. Jalani, and R. Datta, *J. Electrochem. Soc.*, **152**, A1548 (2005).
83. X. Luo, S. Holdcroft, A. Mani, Y. Zhang, and Z. Shi, *Phys. Chem. Chem. Phys.*, **13**, 18055 (2011).
84. E. Quartarone, S. Angioni, and P. Mustarelli, *Materials*, **10**, 687 (2017).
85. F. C. T. OFFICE, *DOE Technical Targets for Polymer Electrolyte Membrane Fuel Cell Components* (Office of energy efficency & renewable energy, ENERGY. GOV) (2018).
86. H. Feng, *Polymer*, **48**, 2988 (2007).
87. B. Jiang, L. Yu, L. Wu, D. Mu, L. Liu, J. Xi, and X. Qiu, *ACS Appl. Mater. Interfaces*, **8**, 12228 (2016).
88. M. Cappadonia, J. W. Erning, S. M. S. Niaki, and U. Stimming, *Solid State Ionics*, **77**, 65 (1995).
89. Y. Sone, P. Ekdunge, and D. Simonsson, *J. Electrochem. Soc.*, **143**, 1254 (1996).
90. L. Maldonado, J. C. Perrin, J. Dillet, and O. Lottin, *J. Membr. Sci.*, **389**, 43 (2012).
91. W. H. Tang, R. Zhang, B. B. Liu, and H. L. Yuan, *J. Appl. Polym. Sci.*, **131** (2014).
92. F. D. Coms, T. J. Fuller, and C. P. Schaffer, *ECS Trans.*, **69**, 189 (2015).
93. W. Xie, R. M. Darling, and M. L. Perry, *J. Electrochem. Soc.*, **163**, A5084 (2016).
94. K. Kidena, T. Ohkubo, N. Takimoto, and A. Ohira, *Eur. Polym. J.*, **46**, 450 (2010).
95. S. A. Berlinger, P. J. Dudenas, A. Bird, X. Chen, G. Freychet, B. D. McCloskey, A. Kusoglu, and A. Z. Weber, *ACS Applied Polymer Materials*, **2**, 5824 (2020).
96. L. M. Onishi, J. M. Prausnitz, and J. Newman, *J. Phys. Chem. B*, **111**, 10166 (2007).
97. J. A. Elliott, S. Hanna, A. M. S. Elliott, and G. E. Cooley, *Macromolecules*, **33**, 4161 (2000).
98. O. Kwon, S. J. Wu, and D. M. Zhu, *J. Phys. Chem. B*, **114**, 14989 (2010).
99. G. M. Divoux, K. A. Finlay, J. K. Park, J.-M. Song, B. Yan, M. Zhang, D. A. Dillard, and R. B. Moore, *ECS Trans.*, **41**, 87 (2011).
100. M. H. Kim, C. J. Glinka, S. A. Grot, and W. G. Grot, *Macromolecules*, **39**, 4775 (2006).
101. P. J. Dudenas and A. Kusoglu, *Macromolecules*, **52**, 7779 (2019).
102. X. Gao et al., *Langmuir* (2020).
103. M. Tesfaye, D. I. Kushner, B. D. McCloskey, A. Z. Weber, and A. Kusoglu, *ACS Macro Lett.*, **7**, 1237 (2018).
104. M. Tesfaye, A. N. MacDonald, P. J. Dudenas, A. Kusoglu, and A. Z. Weber, *Electrochem. Commun.*, **87**, 86 (2018).